HHS Public Access

Author manuscript

Cell Rep. Author manuscript; available in PMC 2022 November 09.

Published in final edited form as:

Cell Rep. 2022 October 25; 41(4): 111521. doi:10.1016/j.celrep.2022.111521.

Lateral septum modulates cortical state to tune responsivity to threat stimuli

Mariko Hashimoto[1,4], **Salvador Ignacio Brito**[1,4], **Anne Venner**[3], **Amanda Loren Pasqualini**[1], **Tracy Lulu Yang**[1], **David Allen**[1], **Patrick Michael Fuller**[3,5], **Todd Erryl Anthony**[1,2,6,*]

[1]F.M. Kirby Neurobiology Center, Boston Children's Hospital and Harvard Medical School, Boston, MA 02115, USA

[2]Departments of Psychiatry and Neurology, Boston Children's Hospital, Boston, MA 02115, USA

[3]Department of Neurology, Beth Israel Deaconess Medical Center and Division of Sleep Medicine, Harvard Medical School, Boston, MA 02215, USA

[4]These authors contributed equally

[5]Present address: Department of Neurological Surgery, UC Davis Health, 4800 Y Street Suite 3740, Sacramento, CA 95817, USA

[6]Lead contact

SUMMARY

Sudden unexpected environmental changes capture attention and, when perceived as potentially dangerous, evoke defensive behavioral states. Perturbations of the lateral septum (LS) can produce extreme hyperdefensiveness even to innocuous stimuli, but how this structure influences stimulus-evoked defensive responses and threat perception remains unclear. Here, we show that *Crhr2*-expressing neurons in mouse LS exhibit phasic activation upon detection of threatening but not rewarding stimuli. Threat-stimulus-driven activity predicts the probability but not vigor or type of defensive behavior evoked. Although necessary for and sufficient to potentiate stimulus-triggered defensive responses, LS^{Crhr2} neurons do not promote specific behaviors. Rather, their stimulation elicits negative valence and physiological arousal. Moreover, LS^{Crhr2} activity tracks brain state fluctuations and drives cortical activation and rapid awakening in the absence of threat. Together, our findings suggest that LS directs bottom-up modulation of cortical function to evoke preparatory defensive internal states and selectively enhance responsivity to threat-related stimuli.

*Correspondence: toddeanthonyphd@gmail.com.

AUTHOR CONTRIBUTIONS

M.H., S.I.B., and A.P. performed photometry and/or optogenetic behavior experiments. M.H. performed rabies tracing. S.I.B. and A.P. performed and analyzed HSV anterograde tracing. T.Y. performed *ex vivo* patch clamp recording and GCaMP imaging. A.V. performed EEG/EMG studies. M.H., S.I.B., A.V., A.P., T.Y., and T.E.A. analyzed the data. D.A. built experimental setups and analysis pipelines for looming and head-fixed recordings. T.E.A. conceived the study and wrote the manuscript.

DECLARATION OF INTERESTS

The authors declare no competing interests.

SUPPLEMENTAL INFORMATION

Supplemental information can be found online at https://doi.org/10.1016/j.celrep.2022.111521.

In brief

Using *in vivo* neural activity recording, optogenetics, and viral-mediated transneuronal anterograde tracing, Hashimoto et al. find that, rather than simply gating behavior, the lateral septum modulates cortical state and responsivity to sensory stimuli to promote preparatory defensive behavioral states associated with heightened reactivity to threat-related cues.

Graphical Abstract:

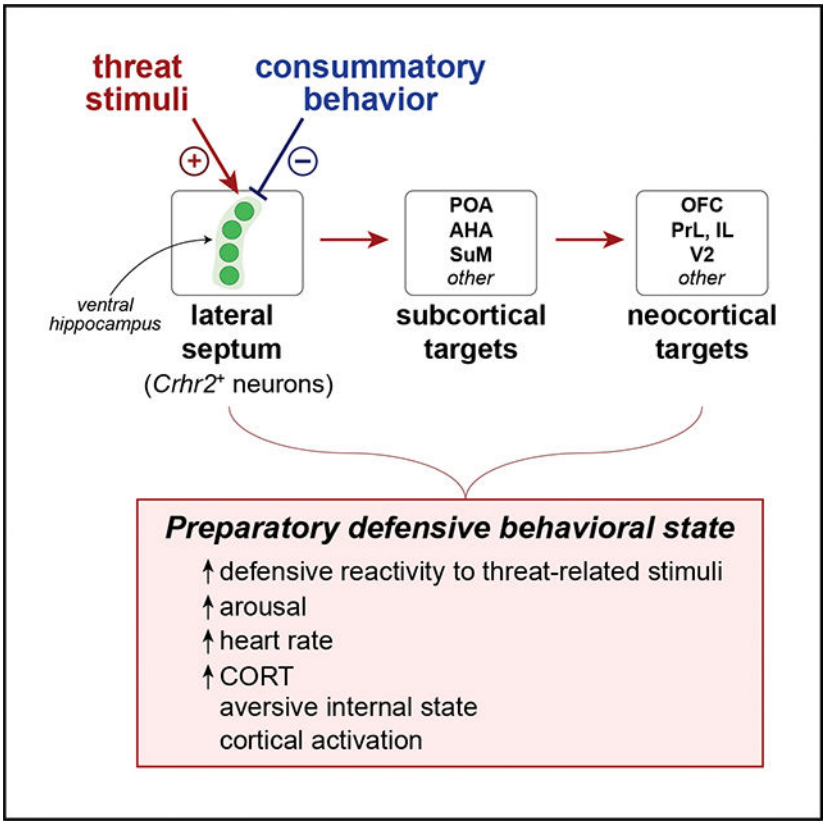

INTRODUCTION

Unexpected salient stimuli drive bottom-up, externally focused vigilant states associated with increased arousal and altered cortical activity patterns (Corbetta and Shulman, 2002; Aston-Jones and Cohen, 2005; Harris and Thiele, 2011; Lee and Dan, 2012). The ability to calibrate responsivity to such stimuli enables defensive behavior to be flexibly tuned according to environmental conditions, internal need states, and/or experience. For example, aversive experience can increase reactivity to threat-related stimuli (Li et al., 2018). However, chronic sensory hypersensitivity in the absence of threat can be maladaptive and is a diagnostic feature of multiple mental illnesses (Freedman et al., 1987; Pitman et al., 2012; Robertson and Baron-Cohen, 2017). Definition of the neural substrates that regulate responsivity to environmental stimuli is fundamental to understanding sensory processing deficits.

The septohippocampal system has long been implicated in gating responses to sensory stimuli. For example, auditory stimuli evoke habituating responses in hippocampal (HPC) neurons (Vinogradova and Brazhnik, 1978; Vinogradova, 2001), and HPC activity is required for suppressing responses to familiar or redundant stimuli (Ackil et al., 1969; Solomon, 1977; Rickert et al., 1978; Kaye and Pearce, 1987). Several lines of evidence suggest that HPC-dependent sensory gating is mediated via descending projections to its primary subcortical target, the lateral septum (LS). LS neurons are phasically activated by salient stimuli (Yadin and Thomas, 1981; Besnard et al., 2019; Wirtshafter and Wilson, 2019; Xu et al., 2019; Azevedo et al., 2020) and exhibit HPC-dependent habituating responses to repeatedly presented unreinforced stimuli (Vinogradova and Brazhnik, 1978). Moreover, lesioning or pharmacologically inactivating the septum (Brady and Nauta, 1953) or LS (Kohler, 1976; Albert and Wong, 1978) can produce extreme sensory hypersensitivity associated with exaggerated stimulus-driven defensive responses and delayed habituation to innocuous stimuli. While such results suggested a role in suppressing defensive responses to salient stimuli (Sheehan et al., 2004), other studies indicate that at least some LS populations may promote threat-related behaviors (Treit and Pesold, 1990; Anthony et al., 2014; Xu et al., 2019). Given the molecular and connectional complexity of the LS (Risold and Swanson, 1997a; 1997b), discrete neuronal cell types may exert distinct influences on sensory-evoked responses. However, the identities and function of the relevant cell types have not been determined.

Several models of LS function have proposed a regulatory “gating” role in which LS output does not directly evoke but rather disinhibits behavior via long-range GABAergic projections to downstream regions involved in locomotion or motivated behavior (Sheehan et al., 2004; Besnard et al., 2019). Related models posit that LS integrates locomotor and/or HPC-derived contextual information to influence action selection through effects on downstream targets (Tingley and Buzsaki, 2020; Wirtshafter and Wilson, 2021). Consistent with this idea, optogenetic stimulation of LS projections to the hypothalamus can modulate avoidance, aggression, locomotion, and food seeking (Anthony et al., 2014; Bender et al., 2015; Wong et al., 2016; Carus-Cadavieco et al., 2017). Notably, electrically stimulating LS can acutely and reversibly alter activity in frontal cortex (Englot et al., 2009) and modulate visual and auditory evoked potentials (Lorens and Brown, 1967; Golden and Lubar, 1971). However, movement itself modulates sensory stimulus-evoked cortical responses (Niell and Stryker, 2010; Lee et al., 2014). It is therefore unclear if LS effects on cortical activity are an indirect consequence of a more proximal function to influence mobility or, alternatively, there are LS subsets that exert direct effects on cortical state independent of movement.

LS neurons that express the type 2 corticotropin-releasing hormone receptor (LS^{Crhr2}) represent a promising entry point for addressing these issues. CRHR2, a G protein-coupled receptor bound by all CRF-related neuropeptide ligands (Henckens et al., 2016), is expressed in a subset of predominantly GABAergic LS neurons (Anthony et al., 2014). Signaling through LS CRHR2 receptors is engaged by aversive experience and regulates multiple threat-related behaviors, including avoidance, neophobia, and hypophagia (Radulovic et al., 1999; Henry et al., 2006; Bakshi et al., 2007; Ohata and Shibasaki, 2011). Pharmacological blockade of LS CRHR2 signaling renders mice resistant to behavioral consequences of acute stress (Radulovic et al., 1999), and LS^{Crhr2} neuronal activity is

required for both induction and maintenance of stress-elicited anxious states (Anthony et al., 2014). Moreover, LS CRHR2 receptors control defensive freezing evoked by aversive stimuli (Bakshi et al., 2002), as well as associative conditioning to such stimuli (Radulovic et al., 1999; Todorovic et al., 2007). LS^{Crhr2} neurons are therefore strong candidates for modulating cognitive and behavioral responses to discrete threat stimuli in a stress-dependent manner. However, neither the *in vivo* neural activity of LS^{Crhr2} neurons nor mechanisms by which they influence defensive behavior have been defined. Here, we addressed this gap using a combination of *in vivo* neural activity recording, optogenetic manipulations, and polysynaptic anterograde transneuronal tracing. Our results suggest a model in which threat-related stimuli activate LS^{Crhr2} neurons, which, in a locomotion-independent manner, elicit preparatory defensive internal states by driving cortical activation to enhance sensory-evoked responses.

RESULTS

LS^{Crhr2} neurons are activated by unexpected and/or threat-associated sensory stimuli but suppressed during consummatory behavior

Recent *in vivo* recording studies implicating LS in spatial cognition and mobility focused on interactions with dorsal HPC (Bender et al., 2015; Tingley and Buzsaki, 2018; Besnard et al., 2019; Wirtshafter and Wilson, 2019, 2020), but ventral HPC also innervates LS (Risold and Swanson, 1996, 1997b). To map hippocampal and other inputs to LS^{Crhr2} neurons, which comprise ~10% of LS cells (Anthony et al., 2014), we performed rabies-mediated monosynaptic transsynaptic retrograde tracing (Wickersham et al., 2007; Wall et al., 2010). Rabies^{+} HPC inputs to LS^{Crhr2} neurons derived primarily from ventral regions, with dense marking observed in deep regions of the CA1 pyramidal layer, oriens, and subiculum (Figure S1). In contrast, few inputs were detected in dorsal HPC, with small numbers of rabies^{+} cells observed in dCA2/3 and none in dCA1. Inputs from outside HPC derived primarily from the hypothalamus, with smaller numbers in the thalamus, nucleus accumbens, and bed nucleus of the stria terminalis (Figure 1A). Together, these data demonstrate that LS^{Crhr2} neurons receive most of their top-down input from ventral HPC, suggesting distinct functional roles for this population compared with LS subsets that receive strong descending input from dorsal HPC.

To define natural activity patterns that underlie LS^{Crhr2} neuronal control of threat-related behavior, we used fiber photometry to record population activity from neurons expressing the calcium indicator GCaMP6s (Chen et al., 2013; Gunaydin et al., 2014) (Figure 1B). *Ex vivo* recordings confirmed that GCaMP6s fluorescence exhibits a linear relationship to spiking in LS^{Crhr2} neurons (Figure S2). Initial recordings revealed robust responses to approach of laboratory personnel (Figure 1C), a stimulus that evoked vigilance and defensive behaviors in septally lesioned animals (Brady and Nauta, 1953). Phasic activation was also evoked by other salient or innately threatening stimuli across multiple modalities, including visual threats, footshock, and loud auditory stimuli (Figures 1D–1F). Notably, repeated stimulus presentations resulted in significantly reduced responses to later exposures that were observed for all modalities tested and not due to photobleaching (Figure 1G; Figure S3). While exposure to unpaired footshocks did not reverse habituation (Figures S3F

and S3G), stable responsivity to an auditory stimulus could be produced if presentation was paired with aversive footshock (Figures 1H–1J). Thus, LS^{Crhr2} responses to sensory stimuli can be modified by aversive associative memory.

To determine whether LS^{Crhr2} neurons respond to rewarding stimuli, water-restricted mice were placed in a chamber with a lick spout delivering a sucrose solution. In contrast to aversive stimuli, sucrose consumption resulted in decreased GCaMP fluorescence for the duration of licking (Figure 2A). Surprisingly, similar decreases occurred when mice consumed a bitter solution (Figure 2B), suggesting this inhibition may facilitate engagement in consummatory behavior rather than reflect detection of rewarding stimuli. To test this idea and dissociate reward from consumption, water-restricted mice were trained daily for 10 days in a task where each trial began with a tone onset indicating water availability 3 s later from a port at one end of the chamber; port entries were monitored via infrared beam breaks (Figures 2C, S4A, and S4B). Early in training (day 2), port entries were accompanied by GCaMP fluorescence decreases regardless of whether or not water reward was available in the port (Figure S4C). However, once mice exhibited behavioral evidence of task learning, fluorescence decreases occurred only when water was available and mice were thirsty (Figures S4D–S4G). Moreover, trial-by-trial fluorescence decreases were related to port entries but not tone onsets (Figures 2D–2F), indicating that activity is inhibited when mice anticipate and/or engage in water consumption, not in response to reward-predictive stimuli. Together, these data demonstrate that LS^{Crhr2} neurons are phasically activated by threat- but not reward-associated sensory stimuli, and are suppressed during consummatory behavior.

Stimulus-driven activation of LS^{Crhr2} neurons occurs upon threat detection and is related to probability but not vigor of defensive responses

To determine how threat-induced activation of LS^{Crhr2} neurons is related to defensive behavior, we further analyzed neural activity and behavioral responses to visual looming stimuli. These overhead expanding black discs mimic approaching aerial predators and elicit robust defensive reactions in mice (Yilmaz and Meister, 2013). Photometry recordings were made in a rectangular arena with a shelter area on one end; entry into a trigger zone in the non-sheltered open region resulted in loom presentation from an overhead monitor but no other aversive stimulus (Figure 3A). The first three presentations of rapidly expanding stimuli elicited a consistent behavioral sequence: initial behavioral inhibition (i.e., suppression of ongoing exploration) indicating threat stimulus detection, followed by flight into the shelter; freezing in the trigger zone or other behaviors (e.g., risk assessment) were observed in some instances (Figure 3B). Loom stimuli robustly activated LS^{Crhr2} neurons upon threat detection irrespective of whether mice exhibited flight or freezing, responses observed at multiple LS recording sites (Figures 3C, 3G and S5D–S5I; Videos S1 and S2). In addition, vigor of flight and subsequent freezing responses were unrelated to the magnitude of evoked neural activity (Figure 3D); neural activity was similarly unrelated to velocity during initial baseline recordings in the absence of threat-related stimuli (Figure S5J).

Stimulus intensity influences perceived threat (Hersman et al., 2020) and modulates latency and vigor of loom-elicited defensive responses (Yilmaz and Meister, 2013; Dunn et al., 2016; Bhattacharyya et al., 2017; von Reyn et al., 2017; Evans et al., 2018). To determine if LS^{Crhr2} neurons are sensitive to threat stimulus intensity, we tested a slowly expanding loom stimulus and found it evoked significantly reduced behavioral and neural responses compared with rapid stimuli (Figures 3E–3G). Importantly, although the magnitude of LS^{Crhr2} responses to loom stimuli was unrelated to behavioral vigor (Figure 3D), it was highly predictive of whether or not a defensive response would occur on a given trial (Figure 3H). Conversely, repeated presentations of loom stimuli resulted in parallel decreases of both behavioral and LS^{Crhr2} neural activity responses (Figure 3I). Moreover, we observed neither defensive nor neural activity responses to expanding white discs (Figure S5), which are not innately threatening (Yilmaz and Meister, 2013). Thus, stimulus-evoked LS^{Crhr2} activity occurs upon threat detection, depends on perceived threat, and is associated with elicitation of defensive internal states but not specific behaviors.

LS^{Crhr2} neuronal activity is necessary for stimulus-triggered defensive behavior and sufficient to drive responses to low-intensity threats

To determine if stimulus-evoked activity causally influences defensive behavior, we first tested effects of optogenetically inhibiting LS^{Crhr2} neurons. An adeno-associated virus (AAV) directing Cre-dependent expression of the inhibitory opsin archaerhodopsin 3.0 (Arch 3.0) was bilaterally injected into LS of *Crhr2*-Cre or nontransgenic control mice; both groups were implanted with fiber optic ferrules and illuminated with 532-nm light during rapid loom stimulus presentations (Figure 4A). We found that photoinhibition of LS^{Crhr2} neurons suppressed defensive responses to rapid loom stimuli, significantly reducing both incidence of flight and maximum velocity within the first 6 s following stimulus onset (Figures 4B and 4C).

Our photometry recordings revealed that the magnitude of stimulus-evoked LS^{Crhr2} activity is related to the probability that a defensive response will be engaged (Figure 3H). We therefore asked if optogenetic stimulation could elicit reactivity to low-intensity stimuli that normally do not evoke defensive responses. Indeed, photostimulating LS^{Crhr2} neurons expressing Channelrhodopsin-2 (ChR2) was sufficient to potentiate defensive responses to slowly expanding loom stimuli, producing flight with increased velocity and greater post-stimulus freezing than controls (Figures 4D–4F; Video S3). Notably, effects of these optogenetic manipulations did not shift defensive responses from one behavior to another (e.g., flight to freezing), but rather altered the probability of a defensive response being exhibited. Moreover, photostimulation inside the looming arena but in the absence of loom stimulus presentations did not significantly alter these behaviors (Figure 4G).

The LS sends GABAergic projections to the hypothalamus proposed to gate motivated behavior and hormonal status via multisynaptic disinhibitory connections (Risold and Swanson, 1997b; Sheehan et al., 2004; Anthony et al., 2014). Accordingly, the above results potentially suggest a gating mechanism in which LS^{Crhr2} activation is permissive (but not instructive) for elicitation of any among a set of defensive behaviors. Such a function could be implemented by disinhibition of downstream effector circuits that actually

drive the responses. If this were the only underlying mechanism by which LS^{Crhr2} neurons influence behavior, photostimulation might be expected to have no acute measurable effects in absence of a threat stimulus. However, we found that photostimulation elicits avoidance in a real-time place aversion assay without altering locomotion (Figure 4H). Similarly, photostimulation suppressed self-initiated burying but not distance traveled in a marble-burying assay (Figure 4I). Thus, LS^{Crhr2} neuronal activation elicits an aversive internal state that can have multiple behavioral consequences, potentiating active or passive defensive responses depending on the situation and on the presence or absence of a discrete threat stimulus.

Polysynaptic anterograde transneuronal tracing indicates that LS^{Crhr2} neurons send indirect projections to discrete neocortical regions

While the above results do not exclude a role for gating, they demonstrate that LS^{Crhr2} activity has acute effects on internal state that can influence responsivity to threat-associated stimuli. In considering mechanisms by which LS^{Crhr2} neurons might produce such effects, we were struck by the prior finding that electrically stimulating LS can acutely and reversibly alter local field potential and cholinergic signaling in frontal cortex (Englot et al., 2009; Li et al., 2015). Moreover, we observed LS^{Crhr2} photometry transients during testing that tracked small head movements resembling risk assessment and that occurred while mice were otherwise immobile (Video S2). Such observations, together with their strong threat-stimulus-driven activation (Figures 1 and 2) and known LS contribution to orienting responses (Kohler, 1976), suggested to us that LS^{Crhr2} neurons might promote bottom-up attention via modulation of cortical function.

The LS^{Crhr2} population is composed primarily of GABAergic neurons that innervate multiple subcortical targets but does not send direct ascending projections to neocortex (Anthony et al., 2014). However, prior studies suggested that LS may modulate cortical state through indirect projections to subcortical arousal systems that in turn innervate neocortical targets (Li et al., 2015; Motelow et al., 2015). To test this idea, we infected LS^{Crhr2} neurons with the transneuronal tracer H129ΔTK-TT (Zemanick et al., 1991; Lo and Anderson, 2011). Following a Cre-mediated recombination event, H129ΔTK-TT expresses the fluorescent reporter tdTomato and becomes replication competent, moving through and marking synaptically connected chains of neurons exclusively in the anterograde direction (Figure 5A). At 1 day post injection (dpi), robust tdTomato was observed only in LS cells surrounding the injection site (Figure 5B; Figures S6A–S6C). By 3 dpi, strong marking was observed in the anterior hypothalamic area and paraventricular nucleus (Figure 5C), regions we previously showed to be downstream of LS^{Crhr2} neurons (Anthony et al., 2014). Notably, dense marking at 3 dpi was also observed in preoptic and supramammillary areas (Figures 5D and 5E), two subcortical regions that influence cortical state (Chung et al., 2017; Pedersen et al., 2017; Yamagata et al., 2021). In contrast, neocortical marking was minimal to undetectable at 3 dpi (Figures 5F–5H). By 5 dpi however, tdTomato^{+} cells were consistently detected in several discrete neocortical regions, including orbitofrontal cortex, prefrontal and infralimbic cortices, and posterior areas that appear to include secondary visual cortex with minimal labeling in V1 (Figures 5I–5K; Figure S6E). Of note, many other neocortical areas lacked detectable viral marking at all time points assayed (e.g.,

somatosensory cortex; Figure S6D). Importantly, tdTomato was undetectable when virus was injected into nontransgenic control animals (not shown). Together, these data indicate that LS^{Crhr2} neurons send indirect projections, routed through subcortical intermediates, to specific frontal and sensory cortical targets (Figure 5L).

LS^{Crhr2} neuronal activity tracks brain state fluctuations independent of movement and promotes physiological arousal

Neuromodulatory populations that regulate cortical function exhibit neural activity correlations with ongoing brain state changes, as indexed by pupil diameter (McGinley et al., 2015; Reimer et al., 2016). We reasoned that, if the LS^{Crhr2} population influences brain state, its activity might similarly track pupillary fluctuations. In fact, simultaneous fiber photometry and pupillometry recordings revealed a striking correlation between LS^{Crhr2} neuronal activity and dynamic pupil diameter changes (Figures 6A and 6B). Importantly, these correlations were independent of movement (Figures 6C–6F), indicating a relationship to ongoing brain state changes rather than to locomotion. In addition, we found that photostimulating LS^{Crhr2} neurons increased pupil dilation and heart rate, demonstrating sufficiency to causally influence these processes (Figures 6G–6I).

LS^{Crhr2} neuronal stimulation drives short-latency cortical activation and persistent brain state changes in the absence of threat

Pupillometry involves head fixation, which can be stressful for mice. The effects of photostimulation on pupil and heart rate during pupillometry might therefore reflect a role for LS^{Crhr2} neurons to modulate the arousing effects of stress while not directly triggering physiological changes. To test whether LS^{Crhr2} neurons can instructively drive cortical activation in the absence of threat, we tested whether photostimulation could produce awakening from sleep in unrestrained animals previously habituated to the test chamber. Mice expressing ChR2:YFP or YFP in LS^{Crhr2} neurons were implanted with electrodes for electroencephalography (EEG) and electromyography (EMG), and subsequently connected to a system for online sleep detection with closed-loop optogenetic stimulation (Figure 7A). Consistently, photostimulation of LS^{Crhr2} neurons was sufficient to trigger awakening from both non-rapid eye movement (NREM) and rapid eye movement (REM) that in some instances occurred within a few hundred milliseconds of light onset (Figures 7B and 7C). Moreover, photostimulation for 50 min (15 Hz, 20-ms pulses, 5 s on, 5 s off) produced wakefulness throughout the stimulation period, followed by sustained reduction of frequencies in the high theta band (6–10 Hz) for 2 h following stimulation offset (Figure S7). Thus, LS^{Crhr2} neural activity is sufficient to trigger acute cortical activation and provoke persistent brain state changes in the absence of discrete threat.

DISCUSSION

The LS has long been implicated in regulating defensive behaviors, but the specific neuronal populations and mechanisms involved have not been resolved. Here, we identify LS^{Crhr2} neurons as a defined neuronal population that responds phasically to sensory stimuli associated with threat but not reward. Activity of these neurons tracks global brain state fluctuations and drives acute physiological arousal, cortical activation, and negative affect.

Further, LS^{Crhr2} neurons are necessary for stimulus-triggered defensive responses and potentiate reactions to mild stimuli while not promoting specific behaviors in the absence of discrete threat stimuli. Thus, in addition to its proposed role as a broadly permissive gate on behavior, our data suggest that the LS instructively evokes preparatory defensive internal states, including both behavioral and physiological components, that prime an animal to rapidly engage appropriate threat responses.

Septal lesions and focal chemical inactivation of LS both produce hyperdefensive phenotypes in which animals exhibit exaggerated responses to mild or innocuous stimuli (Brady and Nauta, 1953; Albert and Wong, 1978; Albert and Chew, 1980). It is therefore counter to expectation that LS contains a threat-stimulus-driven neuronal subset such as LS^{Crhr2} that promotes defensive responses. Similarly, photometry recordings from an LS subdomain anterior to most LS^{Crhr2} neurons also detected threat-related activity, and stimulation of excitatory inputs to this region was aversive and evoked defensive behaviors (Xu et al., 2019). A likely explanation for such apparently contradictory results is that the LS, a large heterogeneous structure (Risold and Swanson, 1997b, a), contains multiple discrete neuronal subsets with distinct effects on threat responding and affect. In fact, stimulation of neurons in posteroventral LS is rewarding and elicits both real-time and conditioned place preference (Mu et al., 2020). Additionally, although LS^{Crhr2} neurons are unresponsive to reward stimuli (Figure 2), electrophysiological recordings in dorsal LS identified cells that fire in response to conditioned reward cues (Wirtshafter and Wilson, 2019). Moreover, although LS^{Crhr2} neurons were inhibited during consummatory behavior (Figure 2) and LS CRHR2 receptors suppress consumption (Bakshi et al., 2007), somatostatin^{+} LS neurons promote food seeking (Carus-Cadavieco et al., 2017). Further genetically based dissection of specific neuronal subsets should clarify the cellular and circuit bases by which LS regulates defensive behavior and valence processing.

Despite the lack of a clear relationship with vigor of freezing or flight behavior, loom-evoked LS^{Crhr2} activation upon threat detection tracked stimulus intensity and strongly predicted probability of a defensive response. Likewise, optogenetically manipulating LS^{Crhr2} cells during loom presentation altered the probability but not type of defensive behavior engaged (Figure 3). Similar characteristics were observed in medial superior colliculus (mSC) neurons proposed to function as threat integrators that evoke escape above a critical threshold (Evans et al., 2018). Thus, LS^{Crhr2} and mSC neurons exhibit similar neural activity relationships to threat intensity and probability of defensive responses while apparently differing in the functional consequences of their output. The identification of loom-responsive thalamic neurons that promote arousal, saliency-enhancing behaviors, and positive affect (Salay et al., 2018) suggests that threat response circuits may be further distinguished according to their associated valence and behavioral strategy evoked (e.g., confrontation versus avoidance).

Although it is unclear how LS^{Crhr2} activity influences cortical state, electrical stimulation of LS can produce acute changes in cortical choline levels (Li et al., 2015). Moreover, LS provides direct input to cholinergic neurons in basal forebrain that are presynaptic to targets in frontal cortex (Gielow and Zaborszky, 2017), and LS^{Crhr2} axons are present in the diagonal band (our unpublished findings). In addition, our viral transneuronal tracing

(Figure 5) indicates that LS^{Crhr2} neurons are mono- and/or poly-synaptically connected with targets in preoptic and supramammillary areas of the hypothalamus, regions known to regulate cortical state (Chung et al., 2017; Pedersen et al., 2017; Yamagata et al., 2021) and to directly or indirectly project to neocortex (Vertes, 1992; Risold et al., 1997). Through multisynaptic LS > hypothalamus > cortex pathways, LS^{Crhr2} neurons might influence interpretation of, and/or sensitivity to, threat-related stimuli by functionally modulating targets in discrete frontal and sensory neocortical regions. Precedent for such an idea comes from work showing that hypothalamic agouti-related peptide-expressing “hunger neurons” send indirect projections to insular cortex that modulate responsivity to food-related cues (Livneh et al., 2017). Other connections may also contribute to LS control of brain state.

We previously reported that LS^{Crhr2} neurons positively regulate circulating corticosteroid levels (Anthony et al., 2014). Importantly, although it takes minutes for corticosterone levels to rise in the blood following stress-induced activation of the HPA axis (Koolhaas et al., 2011), phenotypes reported here (enhanced sensitivity to a low-intensity visual threat, increased arousal and heart rate, cortical activation) could be observed within seconds of optogenetic stimulation. This suggests that LS^{Crhr2} neuron activation evokes behavioral and physiological changes that operate over both short and long timescales to mediate phasic as well as persistent enhancement of defensive responses.

Although there is consensus that LS is an essential regulator of threat responding, studies of the mechanisms involved have focused on different underlying processes. Much current work has addressed LS roles in the integration of spatial and/or locomotor information derived from HPC and hypothalamic inputs (Luo et al., 2011; Bender et al., 2015; Tingley and Buzsaki, 2018; Besnard et al., 2019; Wirtshafter and Wilson, 2019; van der Veldt et al., 2021). Models based on these studies emphasize a key role for LS in promoting contextually appropriate action selection (Tingley and Buzsaki, 2020; Wirtshafter and Wilson, 2021). Importantly, substantial evidence indicates that HPC subserves multiple non-spatial functions relevant to avoiding danger, including episodic memory and event sequencing (Fortin et al., 2002), timing uncertainty (Cavdaroglu et al., 2021), novelty-familiarity discrimination (Rutishauser et al., 2006; Okuyama et al., 2016), and conflict detection and resolution (Gray and McNaughton, 2000; Schumacher et al., 2018). At least some of these functions appear likely to involve HPC projections to LS. For example, habituation of LS responses to repeated unconditioned tone presentations is absent when HPC and LS are disconnected via septo-fimbrial lesions (Vinogradova and Brazhnik, 1978). Related, LS lesions retard habituation of orienting responses to repeated presentations of salient but innocuous stimuli (Kohler, 1976). Moreover, projections from ventral HPC to LS control approach-avoidance conflict behavior in a task involving processing of visuotactile but not spatial cues (Yeates et al., 2022). The extensive molecular and connectional diversity of both HPC and LS (Risold and Swanson, 1996, 1997a; Thompson et al., 2008; Dong et al., 2009; Anthony et al., 2014; Cembrowski et al., 2016; Gergues et al., 2020; García et al., 2021) suggests the possibility of separable hippocamposeptal pathways that control context-action selection, conflict resolution, or stimulus-behavioral state pairing, with intraseptal connections mediating interactions between them. Genetically targeted recordings from defined LS subsets and their HPC inputs will be important for testing this model.

Many neuronal subsets distributed throughout the brain exhibit grossly similar activity patterns and related phenotypes when perturbed as described above for LS^{Crhr2} neurons. For example, electrophysiological recordings showed that norepinephrine neurons in the locus coeruleus (LC-NE) respond phasically to salient stimuli across multiple modalities (Foote et al., 1980; Aston-Jones and Bloom, 1981). Similarly, LC-NE stimulation evokes pupil dilation, rapid awakening, negative affect, and enhanced cortical responses to salient stimuli, and is required for sensory-evoked awakening (Carter et al., 2010; McCall et al., 2015; Vazey et al., 2018; Breton-Provencher and Sur, 2019; Hayat et al., 2020). Related observations in many other populations raise a general question: what is the unique function for different stimulus-driven neuronal populations? At least one distinction may be with respect to valence. For example, cholinergic and noncholinergic neurons in basal forebrain (Lin and Nicolelis, 2008; Hangya et al., 2015) and dorsal raphe dopaminergic neurons (Cho et al., 2017) respond to salient stimuli irrespective of hedonic valence, whereas LS^{Crhr2} neurons are selective for aversive or threatening stimuli (Figures 1 and 2). It is also possible that simultaneous multi-site recordings performed with high temporal resolution would reveal important regional distinctions, such as the precise kinetics of stimulus-driven activity. Alternatively, it could be that many regions perform related computations and produce similar global effects when activated, with the primary functional distinction lying in their inputs and regulation. In particular, as the primary subcortical target of HPC, the LS places stimulus-driven cortical activation and defensive behavior under HPC control. Related, LS^{Crhr2} neurons express *Crhr2* mRNA more highly than any other area of the rodent brain (Van Pett et al., 2000), and receive robust innervation from ventral HPC (Figure S1), a well-known regulator of affective state (Fanselow and Dong, 2010; Strange et al., 2014). As recipients of both vHPC output and stress-activated CRHR2 signaling, our results suggest a model in which LS^{Crhr2} neurons regulate stimulus-driven cortical activation by integrating HPC-derived contextual and mnemonic information with hormonal signaling evoked by recent behavioral challenge. Our findings establish a platform for investigation of hippocamposeptal control of sensory processing by providing a point of entry into a key LS subset. Definition of the circuits through which LS^{Crhr2} neurons regulate cortical state, and their modulation by CRHR2 signaling, will yield important insight into how stressful experiences produce persistent changes in mood and behavior.

Limitations of the study

Neurons expressing the *Crhr2* gene are distributed across several LS subdomains that prior work has shown to be molecularly, connectionally, and functionally distinct. It is therefore possible that LS^{Crhr2} neurons are not functionally homogeneous, and that some population-level neural activity patterns and optogenetic phenotypes reported here are mediated by multiple discrete neuronal cell types that all express the *Crhr2* gene. Follow-up studies using cellular resolution *in vivo* recordings (e.g., microendoscopic calcium imaging), transcriptional profiling (e.g., single-nucleus RNA sequencing), and connectivity-based approaches will be important for determining how the LS^{Crhr2} population controls preparatory defensive internal states.

STAR★METHODS

RESOURCE AVAILABILITY

Lead contact—Further information and requests for resources and reagents should be directed to and will be fulfilled by the lead contact, Todd Anthony: toddeanthonyphd@gmail.com.

Materials availability—This study generated new AAV plasmids (listed in key resources table), which are available upon request to the lead contact.

Data code availability—All data reported in this paper will be shared by the lead contact upon request. All original code (behavior, pupillometry, and neural activity data acquisition and analysis) has been deposited at Zenodo and is publicly available as of the date of publication. DOIs are listed in the key resources table. Any additional information required to reanalyze the data reported in this paper is available from the lead contact upon request.

EXPERIMENTAL MODEL AND SUBJECT DETAILS

All animal care and experimental procedures were approved by the Institutional Animal Care and Use Committee at Boston Children's Hospital or Beth Israel Deaconess Medical Center. Mice were maintained on a 12:12 light dark cycle in constant temperature (22 ± 1°C) and humidity with ad libitum access to food and water. We previously described the generation and characterization of the *Crhr2*α-Cre BAC transgenic line (maintained on FVB/NTac background), which expresses an eGFPCre fusion protein from the start codon in the third exon of the brain-selective alpha-splice variant of the *Crhr2* gene (Anthony et al., 2014). For behavior and imaging experiments, hemizygous transgenic FVB/NTac animals were bred to nontransgenic C57BL/6N mice (Envigo), to generate FVBxB6 F1 hybrids (a.k.a. 'FVBB6F1') transgenics used for testing. Male mice were used to generate all data in the manuscript except photometry recordings during threat conditioning (Figure 1), sucrose/quinine consumption, and reward conditioning (Figure 2), which utilized females (though we note that sex differences were not observed, e.g. males show neural activity decreases during consummatory behavior, and females robustly respond to loom stimuli). After surgical procedures, mice were singly housed; all animals were tested between 12 and 24 weeks of age. Due to toxicity associated with HSV infection, H129ΔTK-TT anterograde tracing was performed using a *Crhr2*-IRES-Cre line (Prescott et al., 2020), JAX stock #033728; the lower efficiency of recombination in this IRES-Cre line (as compared with *Crhr2*α-Cre BAC mice, in which Cre is expressed from the ATG of the *Crhr2*α gene) enabled longer survival times post-injection, facilitating viral spread to higher-order targets. Gene nomenclature is based on the "Guidelines for Nomenclature of Genes, Genetic Markers, Alleles, and Mutations in Mouse and Rat", International Committee on Standardized Genetic Nomenclature for Mice, full details available on Mouse Genome Informatics website.

METHOD DETAILS

Virus injection surgical procedures—All surgery was performed under aseptic conditions and body temperature maintained with a heating pad. Mice were anesthetized

with isoflurane mixed with oxygen (3% for induction, 1.5% for maintenance, 0.8 min−1 oxygen flow rate) and placed in a Model 940 or 1900 digital small-animal stereotax (David Kopf Instruments). Following initial induction, hair was removed from the dorsal surface of the head with hair clippers, ophthalmic ointment applied to the eyes, and the incision area scrubbed with alcohol and betadine. Coordinates used for LS injection were: AP+0.65 mm, ML±0.63 mm, DV−2.7 mm. Virus was backfilled into glass capillaries (tip diameter ~50 mm) and delivered using a nanoliter injector controlled by an ultra microsyringe pump (Nanoliter Injector, 2010 & Micro4, World Precision Instruments) at a flow rate of 30 nL min^{-1}; the pipette was withdrawn at least 3 min after viral injection completion. For fiber photometry, 150 nL of AAV5_CAG(del)-GCaMP6s-FLEx(*loxP*) (Addgene) was unilaterally injected into LS. For optogenetic experiments, 90 nL of AAV5_CAG(del)-Arch3:YFP-FLEx(*loxP*) (custom plasmid), AAV9_CAG(del)-ChR2(H134R):YFP-FLEx(*loxP*) (custom plasmid), or AAV9_CAG(del)-EYFP-FLEx(*loxP*) (custom plasmid) were bilaterally injected into LS. For rabies-mediated monosynaptic retrograde tracing, two vectors (AAV5_CAG(del)-split-TVA:Citrine-FLEx(*loxP*) (custom plasmid) + AAV5_CAG(del)-Rabies G-FLEx(*loxP*) (custom plasmid, cloned by moving RG from pAAV-CA-FLEX-RG (Watabe-Uchida et al., 2012) into CAG(del) promoter-driven AAV vector) were mixed at a 1:9 ratio, and 30 nL of this mixture was unilaterally injected into LS. Two weeks later, 60 nL of EnvA G-Deleted SADB19 Rabies-mCherry virus ((Osakada et al., 2011), packaged by the Salk GT3 Vector Core) was injected into the same site. All custom AAV vectors were packaged by the Boston Children's Hospital Viral Core Facility. For Cre-dependent transsynaptic anterograde tracing, H129ΔTK-TT (60 nL, CNNV) was injected into the LS of *Crhr2*-IRES-Cre mice; animals were perfused at 1–5 days post-injection to enable temporal progression of anterograde viral spread to be mapped.

Optic fiber and head post implantation—Following viral injection, ceramic (optogenetics) or metal (fiber photometry) ferrules with optic fibers (optogenetics: 200mm diameter, 0.37 N.A.; fiber photometry: 400mm diameter, 0.48 N.A.) were implanted into centrolateral LS above *Crhr2*-expressing neurons (AP+0.65mm, ML±0.63mm, DV−2.5mm). The fibers, two small screws and/or custom-made titanium headposts were fixed to the skull using C&B Metabond (Parkell). Appropriate post-surgical analgesia was administered to all mice. Mice were given at least 10 days recovery prior to beginning testing.

Surgical procedures for EEG/EMG recording with optogenetic stimulation—Mice received unilateral injections of 100 nL AAV9_CAG(del)-ChR2:YFP-FLEx(*loxP*) or AAV9_CAG(del)-EGFP-FLEx(*loxP*) into LS. Two weeks later, the EEG/EMG headset was implanted together with an optical fiber above the injection site for optogenetic stimulation. The headstage consisted of a 6-pin connector (Heilind Electronics, catalog #MMX853–43-006–10-001000) soldered to 4 EEG screws (Pinnacle, catalog# 8403) and 2 flexible EMG wire electrodes (Plastics One, catalog #E363). Mice were prepared for surgery as described above and burr holes drilled above the LS for unilateral placement of the optical fiber. Three additional burr holes (0.7 mm diameter) were drilled in the skull: one anterior burr hole was drilled at AP+1.0 mm and ML−1.0 mm and two posterior burr holes were drilled at AP−2.0 and ML±1.0. EEG electrode screws were inserted into the burr holes and an optic fiber was stereotaxically guided into position and fixed in place using dental

cement and cyanoacrylate glue. EMG electrodes were then guided down the back of the neck underneath the trapezius muscle, and the entire assembly was coated in a layer of dental cement for insulation and stability.

Fiber photometry recording—Fiber optic cables (1m, 400μm core, 0.48 NA; Doric Lenses) were coupled to implanted optic fibers with zirconia or bronze sleeves (Doric Lenses). Excitation and emission light was passed through a fluorescence minicube (FMC6_AE(405)_E1(465–480)_F1(500–540)_E2(555–570)_F2(580–680)_S, Doric Lenses). Excitation light (~100 μW) was provided by 405nm and 465nm LEDs (Doric) modulated at 531 or 211 Hz using an RZ5P fiber photometry processor (Tucker-Davis Technologies, TDT) running Synapse, and emission light collected via fluorescence photodetector heads integrated into the minicube (Doric Lenses). Signals were demodulated, digitized at 1 kHz, and acquired via the RZ5P processor. Transistor–transistor logic (TTL) time stamps were used to align the signal, video frames, and experimental stimuli. Photometry recordings were done between 4 and 8 weeks following viral vector injection.

Behavioral procedures—All behavioral testing was performed during the dark cycle; pupillometry and EEG/EMG recording were done during the light cycle. Test equipment was thoroughly cleaned with detergent in between animals.

Threat conditioning

Experiment set-up: Behavioral sessions were performed in a standard operant chamber (Med Associates Inc.) equipped with a house light and tone generator using two different contexts. In context A, mice were placed into a white, cylindrical chamber with a smooth floor, with 1% acetic acid odor and ambient light. Context B contained a square enclosure with an electrical grid floor used to deliver footshock, with 70% ethanol odor and no ambient light. Both chambers contained a speaker on one wall through which auditory stimuli (500 ms pips at 1 Hz, 7.5 kHz for 10 s in total) were delivered at 80dB.

Protocol: On day 1 (pre-exposure, context A), following a 3 min baseline period, mice were presented with four presentations of auditory stimuli with 80 s average pseudorandom ITI (range 70–90 s). On day 2 (conditioning, context B), after a 3min baseline period, mice were conditioned with five CS-US pairings of the auditory stimulus that co-terminated with a 1 s, 0.6 mA DC footshock, with 215 s average pseudorandom ITI (range 200–230 s). On day 3, a tone test was performed in context A, with the same protocol as pre-exposure.

Analysis: All behavioral sessions were conducted, video recorded, and analyzed with Video Freeze software (Med Associates Inc.). Freezing behavior was quantified using motion index, (frame-by-frame mask size difference); freezing bouts were included when motion index was below the threshold for longer than 0.5 s.

Sucrose and quinine consumption

Experiment set-up: Experiments were performed in the same operant chamber described above. A lick-spout (Med Associates) delivering 10% sucrose or 1% quinine was installed at one side of the wall, and licking bouts recorded in Synapse (TDT).

Protocol: All mice were water restricted for at least one week prior to testing, weighed daily, and maintained between 80% and 85% of their body weight throughout the experiments. Following a 5 min baseline period, the lick-spout was inserted into the chamber, which provided either sucrose or quinine. Mice had access to the lick-spout for total of 30 min.

Reward conditioning

Experiment set-up: Behavioral sessions were performed in the same operant chamber as threat conditioning. The chamber contained a water dipper on one wall with an IR-beam at the port to detect entries, and an electrical grid floor to deliver footshock. No odor was applied to the context for reward conditioning. Experiments were controlled by custom-written Med-PC codes, and neural signals, stimuli, and camera recording time were synchronized using the TDT system.

Protocol: All mice were water restricted for at least one week prior to start of training, weighed daily, and maintained in between 80% and 85% of their body weight throughout the experiments. Training sessions consisted of 50 trials of auditory stimuli presentation (500-ms pips at 1 Hz, 7.5 kHz, 80 dB) for 10 s, with water available at the port for the latter 7 s with a 19.8 s average pseudorandom ITI (range 10–29 s). The tone-water association learning was established in stages. On day 1, mice were allowed to freely explore the arena without any footshocks to learn the water availability at the port. From day 2, mild DC footshocks (0.35 mA) were introduced when mice entered the port during the ITI period to facilitate learning. Two seconds following each trial was designated as a ‘safe period’ when no footshocks were applied. All mice trained in this way exhibited evidence of learning after 8 training days.

Analysis: The first 50 trials were used for statistical analysis unless otherwise noted. Learning was assessed using % trial beam break (% of trials out of 50 that mice exhibited a beam-break during water available period) and ITI beam-break count. Mice exhibiting >80% trial beam-break and <25 ITI beam-breaks for three consecutive sessions were considered to have learned the task. “Pre-learning” sessions were taken from Day 2. Mice that did not exhibit learning following 10 days of training were excluded from analysis.

Looming assay

Experimental set-up: Looming assays were performed in a rectangular IR-transparent Perspex arena (W: 45.8 cm × L: 28.8 cm × H: 25.3 cm) with a low roof (W: 12 cm × L: 28.8 cm × H: 17 cm) at one end to create a ‘shelter zone’, and a regular computer monitor mounted above the open area of the arena for visual stimulus presentation. Experiments were recorded at 30 frames per second with two orthogonally positioned near-IR ace GigE cameras (Basler). The illumination level was ~20 lux in the arena, and ~5 lux in the shelter.

The location of the mouse in the arena (X, Y) was tracked online by a custom-written Bonsai program as previously described (Shang et al., 2018), and used to deliver stimuli when the mouse entered the 'trigger zone' (15 cm × 15 cm area under the monitor) by custom-written MATLAB code. Neural signals, stimuli, and camera recording times were synchronized in Synapse (TDT). A gray background was presented on the monitor throughout the experiment, with white or black looming stimuli presented on individual trials. The maximum disk size was set at 60% of the shorter length of the window.

Protocol: Mice were placed in the arena and given 3 min to explore the new environment. This was followed by the presentation of overhead white or black looming visual stimuli of two types: rapid loom - 3x loom stimulus that expands to maximum size in 0.25 s and remains on the monitor for 0.25 s, with 0.5 s interstimulus interval); slow loom - single loom stimulus that expands to maximum size over 3 s and remains on the monitor for 3 s (*see panels in* Figure 3). In a typical experiment, mice were presented first with a white stimulus, which was then followed by a series of black stimuli. As stimulus presentation is self-initiated, the intertrial interval (ITI) varied across trials and mice but was limited to be at least one minute. A typical test session lasted for about 30 min. Note: the predominant defensive response observed to rapid loom stimuli in our animals was flight behavior; use of other stimuli or test conditions (e.g. slow loom stimuli, removing the shelter, or sweeping stimuli (De Franceschi et al., 2016)) did not significantly increase freezing.

For Arch3.0-mediated optogenetic inhibition, mice received bilateral continuous illumination from a 532 nm DPSS laser (Shanghai Laser Optic Century) with a 250 ms ramp down to prevent rebound excitation (modulated with an Arduino board). Light was delivered from 0.5 s prior to the looming stimulus onset and continued for 20 s, and power was 2–3 mW at the fiber tips. Nontransgenic littermates were used as controls.

For ChR2-mediated optogenetic stimulation, mice received bilateral pulsed photostimulation from a 473 nm DPSS laser (SLOC) at 15 Hz (20 ms pulse duration); power was 2–3 mW at the fiber tips. Photostimulation was applied together with loom stimulus onset, and continued for 7 s. To test effects of stimulating in the absence of a loom stimulus, the same 15 Hz photostimulation stimulation was applied when mice entered the trigger zone, but without stimulus presentation on the overhead monitor. Nontransgenic littermates were used as controls.

Analysis: Flight or freeze scoring was done manually by an observer blinded to experimental treatment. A trial was categorized as '*flight*' if mice showed both an acute behavioral response to looming stimulus presentation (typically cessation of ongoing exploratory behavior) and also completed entrance into the shelter within 6 s of stimulus onset. A trial was categorized as '*freeze*' if mice showed a complete absence of movement for longer than 1 s during the 6 s period from the stimulus onset. Trials not categorized as either flight or freeze were scored as '*neither*'. Max velocity was calculated during the first 6 s period from stimulus onset for trials that were categorized as either 'flight' or 'neither'. Freezing was quantified when the mask size difference of frames was below 1.5% for longer than 1 s, and % freezing was calculated for the period of 20 s from stimulus onset for all category trial types.

Real-time place testing—Animals were placed into a custom-made arena (L: 52 cm; W: 25 cm) made from black acrylic with two compartments of equal size (25 × 25 cm), as previously described (Stamatakis and Stuber, 2012). Mice with ChR2:YFP or EYFP expression in LS^{Crhr2} neurons were allowed to freely explore the arena for 30 min. Entry into one compartment triggered bilateral photostimulation (1 or 15 Hz, 20 ms pulse width) while the animal remained in the light-paired chamber; entry into the other chamber terminated photostimulation. The % time spent in stimulation side and distance traveled were quantified using Ethovision XT (Noldus).

Marble burying—Twenty black marbles (1 cm diameter) were arrayed 4×5 on the top of a layer of clean bedding in a shoe box cage (19.5 × 34.5 × 14.5 cm). Patch cords were connected, and mice were placed into the cage and allowed to freely explore for 30 min in the dark while behavior was recorded using IR-sensitive cameras. Photostimulation (473 nm light, 20 msec pulse width, 15 Hz, 12–14 mW at each fiber tip, 5 s ON, 5 s off) was applied throughout the 30 min testing period. The number of marbles buried was counted manually; distance traveled was quantified using Ethovision XT (Noldus).

Pupillometry and heart rate measurements—Mice were head-fixed on a running wheel with a rotary encoder for monitoring locomotion, inside of a sound-attenuating cubicle (Med Associates) under constant illumination. Pupils were illuminated with an infrared LED and video of pupillary fluctuations captured using an FLIR Flea3 USB 3.0 camera at 30 fps. Pupil diameters were extracted in real-time using a custom workflow on Bonsai 2.3 (OpenCV) that thresholded and binarized the pupil videos to determine the largest diameter of the pupil per given frame. Eye blinks were removed post-hoc using a custom MATLAB code.

To test effects of optogenetic stimulation on pupil and heart rate, mice were head-fixed on the pupil rig, connected bilaterally to optical patch cords, and fitted with a pulse oximeter collar (MouseOx Plus, Starr Life Sciences). At the beginning of each experiment, ambient light in the test cubicle was briefly turned off to determine the maximum pupil diameter per animal. Mice were given a 10 min baseline period to acclimate to the wheel. Bilateral photostimulation (473 nm, 10 s activation, 15 Hz, 20 ms pulse width, 6 mW at fiber tips) was then applied when the pupil diameter dropped below 60% of the maximum pupil diameter with a minimum ITI of 60 s per trial. Analysis was done using the first 5 trials of each experiment. Nontransgenic littermates were used as controls.

Optogenetic stimulation during NREM or REM sleep—Four weeks after viral vector injection (Cre-dependent ChR2:YFP, experimental group; Cre-dependent EYFP, control group), mice were transferred to a new home cage, adapted for connection of EEG/EMG and fiber optic patch cables, and placed in the recording chamber. Mice were habituated to these conditions for a period of two days before commencing experiments. Cortical EEG (ipsilateral frontoparietal leads) and EMG signals were amplified x5000 (AM Systems, Model 3600) and digitized with a resolution of 500 Hz using a Micro 1401–3 (Cambridge Electronic Design). All mice underwent testing in the following order:

1. Baseline EEG/EMG recordings from ZT 3–9.

2. Brief recurrent optogenetic stimulation during NREM sleep at ZT 3–9. A modified open-source Online Sleep Detection script (Spike 2, Cambridge Electronic Design, source code available from Cambridge Electronic Design website) was used to detect when mice had been in NREM sleep for at least 20 s, which triggered administration of optogenetic stimuli (10 s duration,15 Hz, 20 ms pulse lengths; 473 nm light, 12–15 mW power at fiber tip) with a minimum of 3 min between each stimulus.

3. Brief recurrent optogenetic stimulation during REM sleep at ZT 0–9. The closed-loop online sleep detection script was used to administer optogenetic stimuli (10 s duration, 15 Hz, 20 ms pulse lengths; 473 nm light pulse at 12–15 mW power at the fiber tip) when REM sleep was detected for at least 20 s, with a minimum of 3 min between each stimulus.

Histological and immunostaining procedures—Mice were anesthetized with ketamine and xylazine dilution, and sequentially perfused with saline and phosphate buffered saline (PBS) containing 4% paraformaldehyde (PFA). Brains were removed and incubated in PBS containing 4% PFA overnight on a rocking platform at 4°C. For vibratome sectioning, brains were sectioned at 100 μm thickness and fluorescent imaging performed on upright epifluorescent or confocal microscopes (Zeiss Axioplan or LSM700). For H129ΔTK-TT tracing, sections were immunostained for tdTomato using a polyclonal rabbit anti-RFP primary antibody (MBL cat #PM005), followed by a donkey anti-rabbit Alexa 647 secondary antibody (Jackson Immunoresearch). For microtome sectioning, brains were incubated in 20% sucrose at 4°C until they sank, sectioned at 40 μm, mounted onto poly-L-lysine coated slides, and allowed to dry overnight before being imaged on an Olympus BX61VS slide scanner. Mice in which optical fiber placement was not positioned over the LS were discarded from the analysis.

Fiber photometry analysis—Both 465 nm and 405 nm signals were downsampled to 30 Hz (i.e. sampling rate of behavioral video recordings) and detrended by subtracting the best-fit exponential trace across the entire fluorescence time series to correct for slow bleaching artifacts, as previously described (Kim et al., 2016). We then calculated $\Delta F/F = (F - F_0)/F_0$, where F_0 = the 10th percentile across the detrended time series. Signals in the 405 nm channel were used only for removing trials with significant motion artifacts, not for processing GCaMP traces. Statistical analyses of neural activity are reported as normalized activity (Z score transformation). The ΔF/F time course was Z-scored by subtracting the mean of all data within the 50^{th} percentile, and dividing by the standard deviation of all data with the 50^{th} percentile. Peaks (significant increases in activity) were defined as time points when the z-scored ΔF/F was >1.65 (Fadok et al., 2017), or >2 standard deviations ($p < 0.05$) for a one-tailed 95% confidence interval. Peak AUC was calculated as the area in between the signal and Z score = 1.65, and peak duration was calculated as the length of peak.

Pupillometry analysis—Pupil signals were filtered using a second order butterworth bandpass filter with cutoff frequencies of 0.05 Hz and 1 Hz as described (Breton-Provencher and Sur, 2019). Z-scored dF/F photometry traces were lowpass filtered with a cutoff frequency of 2 Hz. Normalized cross-correlations were then calculated on these two filtered

signals across 13 animals imaged using MATLAB cross correlation functions. Coherence analysis was done on unfiltered pupil and z-scored dF/F signals using MATLAB.

A custom MATLAB code was used to extract individual pupil bouts per recording session for each animal. In short, pupillometry traces were bandpass filtered as described above. Each trace was then z-scored, and a threshold of 0.5 Z score used to determine indices where pupil bouts occurred. These indices were then used to determine the onset of candidate pupil bouts on the original pupillometry trace; candidate pupil bouts shorter than 1 s in duration from onset to offset were removed from analysis. Pupil bout onset indices were then used to extract corresponding fiber photometry and velocity onsets from each aligned time series data. Delta z-scored dF/F across 13 animals was calculated by subtracting the mean z-scored dF/F signal 2 s prior to pupil onset from the z-scored dF/F signal 2 s post pupil onset (post-pre). The same pupil bout onset indices were used on circularly shuffled photometry data (10 s offset) to generate shuffled delta z-scored dF/F calculations.

To analyze effects of optogenetic stimulation, pupillometry traces were first processed using a lowpass filter with a 2 Hz cutoff frequency. To calculate mean pupil delta change, each trial was normalized to the mean pupil diameter 2 s prior to laser stimulation. To account for the slow kinetics of pupil dilation after stimulus presentation, we calculated the mean pupil diameter during the 5 s window 2 s after laser stimulation. Heart rate was processed using the same parameters as pupil described above. Mean heart rate change was calculated as the difference between the second period prior to stimulation versus the 5 s window immediately following onset of laser stimulation.

Sleep scoring and EEG/EMG analysis—Sleep scoring was carried out using Spike 2 (Cambridge Electronic Design) by an investigator blinded to the recording conditions. Polysomnographic records were visually scored in 5 s epochs for wakefulness (W), rapid eye movement (REM) and non-REM (NREM) sleep. The latency to wake and length of wake episodes following optogenetic stimulation were calculated and exported from Spike for visualization using custom-written Python script.

To perform an EEG power spectrum analysis of the chronic (50 min) stimulation data, a Fast Fourier Transform (FFT) routine using a Hanning window of 1024 data points was applied to the EEG signal in the two hours post-experimental condition (i.e. 2 h immediately after cessation of stimulation). Epochs containing artifacts occurring during active wake (with large movements) or containing two vigilance states were visually identified and omitted from the spectral analysis. The data were normalized by expressing each frequency bin as a percentage relative to the same bin in pre-experimental condition (i.e. 2 h immediately prior to the chronic optogenetic stimulus) from the same mouse. To analyze the EEG frequency bands, relative power bins were summed in δ = 0.5–4 Hz, θ = 4–6 Hz, Θ = 6–10 Hz, α = 10–20 Hz.

Electrophysiological slice recordings—Mice unilaterally injected in LS with AAV5_CAG(del)-Arch3:YFP-FLEx(*loxP*) or AAV5_CAG(del)-GCaMP6s-FLEx(*loxP*) were euthanized and perfused transcardially with ice-cold glycerol-based artificial cerebrospinal fluid solution (G-ACSF) composed of (in mM): 252 glycerol, 2.5 KCl, 1.2 NaH_2PO_4, 1.2

$MgCl_2$, 2.4 $CaCl_2$, 26 $NaHCO_3$, 20 glucose and oxygenated with 95% O_2/5% CO_2. Brains were coronally sectioned (250 μm) on a Leica VT1200S vibratome in chilled, oxygenated G-ACSF. Slices were allowed to recover for 90 min at 32°C in oxygenated ACSF composed of (in mM): 125 NaCl, 2.5 KCl, 1.2 NaH_2PO_4, 1.2 $MgCl_2$, 2.4 $CaCl_2$, 26 $NaHCO_3$, 20 glucose. Slices were then transferred to room temperature oxygenated ACSF until recording.

Recordings were performed at 32°C using a Multiclamp 700B amplifier and a Digidata 1550B digitizer (Molecular Devices). Arch3:YFP$^+$ or GCaMP6s$^+$ neurons were visualized via IR-DIC and fluorescence microscopy. Glass pipettes (7–9 MΩ) for whole-cell recordings were filled with internal recording solution composed of (in mM): 135 K-gluconate, 5 KCl, 5 EGTA, 10 HEPES, 0.5 $CaCl_2$-$2H_2O$, 2 ATP-Mg, 0.1 GTP-Na_2, pH 7.2, 292 mosM. Bridge balance was applied to current clamp recordings. Series resistance was <25 MΩ. Data were sampled at 10 kHz, filtered at 3 kHz, imported into MATLAB using the Transalyzer abf2load function (Plesa and Dekker, 2015), and analyzed with custom MATLAB code. Illumination of whole-cell patch clamped Arch3:YFP$^+$ LS^{Crhr2} neurons ($n = 5$) with 532 nm light (3 mW, 20 s sweeps, 250ms ramp down at light offset) drove robust currents (steady state 159.9 ± 25.7 pA) and induced hyperpolarization (steady state −8.9 ± 1.6 mV) in the absence of rebound firing at light offset. Our previous *ex vivo* whole cell recordings demonstrated that ChR2 mediates efficient photostimulation of LS^{Crhr2} neurons (Anthony et al., 2014); in brief, we showed that: *a)* LS^{Crhr2} neurons photostimulated at frequencies up to 15 Hz exhibit a high percentage of successful light-evoked action potentials (~80%) across multiple sweeps; *b)* 15 Hz photostimulation using a 5 s ON 5 s OFF protocol (as used here) evokes efficient inhibitory post-synaptic currents in monosynaptic target neurons over multiple sweeps; and *c)* this same protocol evokes efficient firing from LS^{Crhr2} neurons recorded in cell-attached configuration over 30 min.

QUANTIFICATION AND STATISTICAL ANALYSIS—All statistical tests were carried out using Prism (GraphPad) and details provided in the figure legends. In all cases, values showing $p < 0.05$ were considered significant. Sample size and power calculations were performed post hoc using PS Power and Sample Size Calculations by W. Dupont and W. Plummer (http://biostat.mc.vanderbilt.edu/wiki/Main/PowerSampleSize), using means and standard deviations derived from our analysis. All experimental data were subject to histological validation. Data were excluded if the conditions of the histological validation were not met (e.g. optical fiber was not correctly positioned above the LS). Sample sizes reported in the manuscript reflect only data that was confirmed by histological validation.

Supplementary Material

Refer to Web version on PubMed Central for supplementary material.

ACKNOWLEDGMENTS

We thank Gord Fishell and Mark Andermann for comments on the manuscript and members of the Anthony lab for helpful discussions during the course of this work. We also thank the BCH IDDRC Cellular Imaging Core, funded by NIH P50 HD105351 and S10OD016453, as well as Ofer Mazor and Pavel Gorelik of the Harvard Medical School Research Instrumentation Core Facility for assistance in instrument design and fabrication. H129Δ-TK-TT virus was obtained from the CNNV, supported by NIH Virus Center grant #P40OD 010996. Authors were supported by a William Randolph Hearst Fellowship (M.H.), Ford Foundation Fellowship (S.I.B.), Sleep Research

Society grant CDA 016-JP-17 (A.V.), NS073613, NS092652, and NS103161 (P.M.F.), and the National Institute of Mental Health (#1R01MH117421-01A1), Whitehall Foundation, Charles Hood Foundation, Tommy Fuss Center for Neuropsychiatric Disease Research, Harvard NeuroDiscovery Center, Harvard University Milton Fund, and Harvard Brain Initiative (T.E.A.).

REFERENCES

Ackil JE, Mellgren RL, Halgren C, and Frommer GP (1969). Effects of CS preexposures on avoidance learning in rats with hippocampal lesions. J. Comp. Physiol. Psychol. 69, 739–747. [PubMed: 5359148]

Albert DJ, and Chew GL (1980). The septal forebrain and the inhibitory modulation of attack and defense in the rat. Behav. Neural. Biol. 30, 357–388. [PubMed: 7013753]

Albert DJ, and Wong RC (1978). Hyperreactivity, muricide, and intraspecific aggression in the rat produced by infusion of local anesthetic into the lateral septum or surrounding areas. J. Comp. Physiol. Psychol. 92, 1062–1073. [PubMed: 573285]

Anthony TE, Dee N, Bernard A, Lerchner W, Heintz N, and Anderson DJ (2014). Control of stress-induced persistent anxiety by an extra-amygdala septohypothalamic circuit. Cell 156, 522–536. [PubMed: 24485458]

Aston-Jones G, and Bloom FE (1981). Norepinephrine-containing locus coeruleus neurons in behaving rats exhibit pronounced responses to non-noxious environmental stimuli. J. Neurosci. 1, 887–900. [PubMed: 7346593]

Aston-Jones G, and Cohen JD (2005). An integrative theory of locus coeruleus-norepinephrine function: adaptive gain and optimal performance. Annu. Rev. Neurosci. 28, 403–450. [PubMed: 16022602]

Azevedo EP, Tan B, Pomeranz LE, Ivan V, Fetcho R, Schneeberger M, Doerig KR, Liston C, Friedman JM, and Stern SA (2020). A limbic circuit selectively links active escape to food suppression. Elife 9, e58894. [PubMed: 32894221]

Bakshi VP, Newman SM, Smith-Roe S, Jochman KA, and Kalin NH (2007). Stimulation of lateral septum CRF2 receptors promotes anorexia and stress-like behaviors: functional homology to CRF1 receptors in basolateral amygdala. J. Neurosci. 27, 10568–10577. [PubMed: 17898228]

Bakshi VP, Smith-Roe S, Newman SM, Grigoriadis DE, and Kalin NH (2002). Reduction of stress-induced behavior by antagonism of corticotropin-releasing hormone 2 (CRH2) receptors in lateral septum or CRH1 receptors in amygdala. J. Neurosci. 22, 2926–2935. [PubMed: 11923457]

Bender F, Gorbati M, Cadavieco MC, Denisova N, Gao X, Holman C, Korotkova T, and Ponomarenko A (2015). Theta oscillations regulate the speed of locomotion via a hippocampus to lateral septum pathway. Nat. Commun. 6, 8521. [PubMed: 26455912]

Besnard A, Gao Y, TaeWoo Kim M, Twarkowski H, Reed AK, Langberg T, Feng W, Xu X, Saur D, Zweifel LS, et al. (2019). Dorsolateral septum somatostatin interneurons gate mobility to calibrate context-specific behavioral fear responses. Nat. Neurosci. 22, 436–446. [PubMed: 30718902]

Bhattacharyya K, McLean DL, and MacIver MA (2017). Visual threat assessment and reticulospinal encoding of calibrated responses in larval zebrafish. Curr. Biol. 27, 2751–2762.e6. [PubMed: 28889979]

Brady JV, and Nauta WJ (1953). Subcortical mechanisms in emotional behavior: affective changes following septal forebrain lesions in the albino rat. J. Comp. Physiol. Psychol. 46, 339–346. [PubMed: 13109048]

Breton-Provencher V, and Sur M (2019). Active control of arousal by a locus coeruleus GABAergic circuit. Nat. Neurosci. 22, 218–228. [PubMed: 30643295]

Carter ME, Yizhar O, Chikahisa S, Nguyen H, Adamantidis A, Nishino S, Deisseroth K, and de Lecea L (2010). Tuning arousal with optogenetic modulation of locus coeruleus neurons. Nat. Neurosci. 13, 1526–1533. [PubMed: 21037585]

Carus-Cadavieco M, Gorbati M, Ye L, Bender F, van der Veldt S, Kosse C, Börgers C, Lee SY, Ramakrishnan C, Hu Y, et al. (2017). Gamma oscillations organize top-down signalling to hypothalamus and enable food seeking. Nature 542, 232–236. [PubMed: 28146472]

Çavdaroğlu B, Riaz S, Shi Y, Balcı F, and Ito R (2021). The ventral hippocampus CA3 is critical in regulating timing uncertainty in temporal decision-making. Cell Rep. 34, 108694. [PubMed: 33535032]

Cembrowski MS, Bachman JL, Wang L, Sugino K, Shields BC, and Spruston N (2016). Spatial gene-expression gradients underlie prominent heterogeneity of CA1 pyramidal neurons. Neuron 89, 351–368. [PubMed: 26777276]

Chen TW, Wardill TJ, Sun Y, Pulver SR, Renninger SL, Baohan A, Schreiter ER, Kerr RA, Orger MB, Jayaraman V, et al. (2013). Ultrasensitive fluorescent proteins for imaging neuronal activity. Nature 499, 295–300. [PubMed: 23868258]

Cho JR, Treweek JB, Robinson JE, Xiao C, Bremner LR, Greenbaum A, and Gradinaru V (2017). Dorsal raphe dopamine neurons modulate arousal and promote wakefulness by salient stimuli. Neuron 94, 1205–1219.e8. [PubMed: 28602690]

Chung S, Weber F, Zhong P, Tan CL, Nguyen TN, Beier KT, Hörmann N, Chang WC, Zhang Z, Do JP, et al. (2017). Identification of preoptic sleep neurons using retrograde labelling and gene profiling. Nature 545, 477–481. [PubMed: 28514446]

Corbetta M, and Shulman GL (2002). Control of goal-directed and stimulus-driven attention in the brain. Nat. Rev. Neurosci. 3, 201–215. [PubMed: 11994752]

De Franceschi G, Vivattanasarn T, Saleem AB, and Solomon SG (2016). Vision guides selection of freeze or flight defense strategies in mice. Curr. Biol. 26, 2150–2154. [PubMed: 27498569]

Dong HW, Swanson LW, Chen L, Fanselow MS, and Toga AW (2009). Genomic-anatomic evidence for distinct functional domains in hippocampal field CA1. Proc. Natl. Acad. Sci. USA 106, 11794–11799. [PubMed: 19561297]

Dunn TW, Gebhardt C, Naumann EA, Riegler C, Ahrens MB, Engert F, and Del Bene F (2016). Neural circuits underlying visually evoked escapes in larval zebrafish. Neuron 89, 613–628. [PubMed: 26804997]

Englot DJ, Modi B, Mishra AM, DeSalvo M, Hyder F, and Blumenfeld H (2009). Cortical deactivation induced by subcortical network dysfunction in limbic seizures. J. Neurosci. 29, 13006–13018. [PubMed: 19828814]

Evans DA, Stempel AV, Vale R, Ruehle S, Lefler Y, and Branco T (2018). A synaptic threshold mechanism for computing escape decisions. Nature 558, 590–594. [PubMed: 29925954]

Fadok JP, Krabbe S, Markovic M, Courtin J, Xu C, Massi L, Botta P, Bylund K, Müller C, Kovacevic A, et al. (2017). A competitive inhibitory circuit for selection of active and passive fear responses. Nature 542, 96–100. [PubMed: 28117439]

Fanselow MS, and Dong HW (2010). Are the dorsal and ventral hippocampus functionally distinct structures? Neuron 65, 7–19. [PubMed: 20152109]

Foote SL, Aston-Jones G, and Bloom FE (1980). Impulse activity of locus coeruleus neurons in awake rats and monkeys is a function of sensory stimulation and arousal. Proc. Natl. Acad. Sci. USA 77, 3033–3037. [PubMed: 6771765]

Fortin NJ, Agster KL, and Eichenbaum HB (2002). Critical role of the hippocampus in memory for sequences of events. Nat. Neurosci. 5, 458–462. [PubMed: 11976705]

Freedman R, Adler LE, Gerhardt GA, Waldo M, Baker N, Rose GM, Drebing C, Nagamoto H, Bickford-Wimer P, and Franks R (1987). Neurobiological studies of sensory gating in schizophrenia. Schizophr. Bull. 13, 669–678. [PubMed: 2894074]

García MT, Stegmann SK, Lacey TE, Reid CM, Hrvatin S, Weinreb C, Adam MA, Aurel Nagy M, and Harwell CC (2021). Transcriptional profiling of sequentially generated septal neuron fates. Preprint at bioRxiv. 10.1101/2021.06.29.450296.

Gergues MM, Han KJ, Choi HS, Brown B, Clausing KJ, Turner VS, Vainchtein ID, Molofsky AV, and Kheirbek MA (2020). Circuit and molecular architecture of a ventral hippocampal network. Nat. Neurosci. 23, 1444–1452. [PubMed: 32929245]

Gielow MR, and Zaborszky L (2017). The input-output relationship of the cholinergic basal forebrain. Cell Rep. 18, 1817–1830. [PubMed: 28199851]

Golden GH, and Lubar JF (1971). Effect of septal and fimbrial stimulation on auditory and visual cortical evoked potentials in the cat. Exp. Neurol. 30, 389–402. [PubMed: 5554232]

Gray JA, and McNaughton N (2000). The Neuropsychology of Anxiety : An Enquiry into the Functions of the Septo-Hippocampal System, Second Edition (Oxford University Press).

Gunaydin LA, Grosenick L, Finkelstein JC, Kauvar IV, Fenno LE, Adhikari A, Lammel S, Mirzabekov JJ, Airan RD, Zalocusky KA, et al. (2014). Natural neural projection dynamics underlying social behavior. Cell 157, 1535–1551. [PubMed: 24949967]

Hangya B, Ranade SP, Lorenc M, and Kepecs A (2015). Central cholinergic neurons are rapidly recruited by reinforcement feedback. Cell 162, 1155–1168. [PubMed: 26317475]

Harris KD, and Thiele A (2011). Cortical state and attention. Nat. Rev. Neurosci. 12, 509–523. [PubMed: 21829219]

Hayat H, Regev N, Matosevich N, Sales A, Paredes-Rodriguez E, Krom AJ, Bergman L, Li Y, Lavigne M, Kremer EJ, et al. (2020). Locus coeruleus norepinephrine activity mediates sensory-evoked awakenings from sleep. Sci. Adv. 6, eaaz4232.

Henckens MJAG, Deussing JM, and Chen A (2016). Region-specific roles of the corticotropin-releasing factor-urocortin system in stress. Nat. Rev. Neurosci. 17, 636–651. [PubMed: 27586075]

Henry B, Vale W, and Markou A (2006). The effect of lateral septum corticotropin-releasing factor receptor 2 activation on anxiety is modulated by stress. J. Neurosci. 26, 9142–9152. [PubMed: 16957071]

Hersman S, Allen D, Hashimoto M, Brito SI, and Anthony TE (2020). Stimulus salience determines defensive behaviors elicited by aversively conditioned serial compound auditory stimuli. Elife 9, e53803. [PubMed: 32216876]

Kaye H, and Pearce JM (1987). Hippocampal lesions attenuate latent inhibition and the decline of the orienting response in rats. Q. J. Exp. Psychol. B 39, 107–125. [PubMed: 3602420]

Kim CK, Yang SJ, Pichamoorthy N, Young NP, Kauvar I, Jennings JH, Lerner TN, Berndt A, Lee SY, Ramakrishnan C, et al. (2016). Simultaneous fast measurement of circuit dynamics at multiple sites across the mammalian brain. Nat. Methods 13, 325–328. [PubMed: 26878381]

Köhler C (1976). Habituation of the orienting response after medial and lateral septal lesions in the albino rat. Behav. Biol. 16, 63–72. [PubMed: 1252219]

Koolhaas JM, Bartolomucci A, Buwalda B, de Boer SF, Flügge G, Korte SM, Meerlo P, Murison R, Olivier B, Palanza P, et al. (2011). Stress revisited: a critical evaluation of the stress concept. Neurosci. Biobehav. Rev. 35, 1291–1301. [PubMed: 21316391]

Lee AM, Hoy JL, Bonci A, Wilbrecht L, Stryker MP, and Niell CM (2014). Identification of a brainstem circuit regulating visual cortical state in parallel with locomotion. Neuron 83, 455–466. [PubMed: 25033185]

Lee SH, and Dan Y (2012). Neuromodulation of brain states. Neuron 76, 209–222. [PubMed: 23040816]

Li L, Feng X, Zhou Z, Zhang H, Shi Q, Lei Z, Shen P, Yang Q, Zhao B, Chen S, et al. (2018). Stress accelerates defensive responses to looming in mice and involves a locus coeruleus-superior colliculus projection. Curr. Biol. 28, 859–871.e5. [PubMed: 29502952]

Li W, Motelow JE, Zhan Q, Hu YC, Kim R, Chen WC, and Blumenfeld H (2015). Cortical network switching: possible role of the lateral septum and cholinergic arousal. Brain Stimul. 8, 36–41. [PubMed: 25440289]

Lin SC, and Nicolelis MAL (2008). Neuronal ensemble bursting in the basal forebrain encodes salience irrespective of valence. Neuron 59, 138–149. [PubMed: 18614035]

Livneh Y, Ramesh RN, Burgess CR, Levandowski KM, Madara JC, Fenselau H, Goldey GJ, Diaz VE, Jikomes N, Resch JM, et al. (2017). Homeostatic circuits selectively gate food cue responses in insular cortex. Nature 546, 611–616. [PubMed: 28614299]

Lo L, and Anderson DJ (2011). A Cre-dependent, anterograde transsynaptic viral tracer for mapping output pathways of genetically marked neurons. Neuron 72, 938–950. [PubMed: 22196330]

Lorens SA, and Brown TS (1967). Influence of stimulation of the septal area on visual evoked potentials. Exp. Neurol. 17, 86–90. [PubMed: 4163569]

Luo AH, Tahsili-Fahadan P, Wise RA, Lupica CR, and Aston-Jones G (2011). Linking context with reward: a functional circuit from hippocampal CA3 to ventral tegmental area. Science 333, 353–357. [PubMed: 21764750]

McCall JG, Al-Hasani R, Siuda ER, Hong DY, Norris AJ, Ford CP, and Bruchas MR (2015). CRH engagement of the locus coeruleus noradrenergic system mediates stress-induced anxiety. Neuron 87, 605–620. [PubMed: 26212712]

McGinley MJ, Vinck M, Reimer J, Batista-Brito R, Zagha E, Cadwell CR, Tolias AS, Cardin JA, and McCormick DA (2015). Waking state: rapid variations modulate neural and behavioral responses. Neuron 87, 1143–1161. [PubMed: 26402600]

Motelow JE, Li W, Zhan Q, Mishra AM, Sachdev RNS, Liu G, Gummadavelli A, Zayyad Z, Lee HS, Chu V, et al. (2015). Decreased subcortical cholinergic arousal in focal seizures. Neuron 85, 561–572. [PubMed: 25654258]

Mu MD, Geng HY, Rong KL, Peng RC, Wang ST, Geng LT, Qian ZM, Yung WH, and Ke Y (2020). A limbic circuitry involved in emotional stress-induced grooming. Nat. Commun. 11, 2261. [PubMed: 32385304]

Niell CM, and Stryker MP (2010). Modulation of visual responses by behavioral state in mouse visual cortex. Neuron 65, 472–479. [PubMed: 20188652]

Ohata H, and Shibasaki T (2011). Involvement of CRF2 receptor in the brain regions in restraint-induced anorexia. Neuroreport 22, 494–498. [PubMed: 21666520]

Okuyama T, Kitamura T, Roy DS, Itohara S, and Tonegawa S (2016). Ventral CA1 neurons store social memory. Science 353, 1536–1541. [PubMed: 27708103]

Osakada F, Mori T, Cetin AH, Marshel JH, Virgen B, and Callaway EM (2011). New rabies virus variants for monitoring and manipulating activity and gene expression in defined neural circuits. Neuron 71, 617–631. [PubMed: 21867879]

Pedersen NP, Ferrari L, Venner A, Wang JL, Abbott SBG, Vujovic N, Arrigoni E, Saper CB, and Fuller PM (2017). Supramammillary glutamate neurons are a key node of the arousal system. Nat. Commun. 8, 1405. [PubMed: 29123082]

Pitman RK, Rasmusson AM, Koenen KC, Shin LM, Orr SP, Gilbertson MW, Milad MR, and Liberzon I (2012). Biological studies of post-traumatic stress disorder. Nat. Rev. Neurosci. 13, 769–787. [PubMed: 23047775]

Plesa C, and Dekker C (2015). Data analysis methods for solid-state nanopores. Nanotechnology 26, 084003. [PubMed: 25648179]

Prescott SL, Umans BD, Williams EK, Brust RD, and Liberles SD (2020). An airway protection program revealed by sweeping genetic control of vagal afferents. Cell 181, 574–589.e14. [PubMed: 32259485]

Radulovic J, Rühmann A, Liepold T, and Spiess J (1999). Modulation of learning and anxiety by corticotropin-releasing factor (CRF) and stress: differential roles of CRF receptors 1 and 2. J. Neurosci. 19, 5016–5025. [PubMed: 10366634]

Reimer J, McGinley MJ, Liu Y, Rodenkirch C, Wang Q, McCormick DA, and Tolias AS (2016). Pupil fluctuations track rapid changes in adrenergic and cholinergic activity in cortex. Nat. Commun. 7, 13289. [PubMed: 27824036]

Rickert EJ, Bennett TL, Lane P, and French J (1978). Hippocampectomy and the attenuation of blocking. Behav. Biol. 22, 147–160. [PubMed: 626616]

Risold PY, and Swanson LW (1996). Structural evidence for functional domains in the rat hippocampus. Science 272, 1484–1486. [PubMed: 8633241]

Risold PY, and Swanson LW (1997a). Chemoarchitecture of the rat lateral septal nucleus. Brain Res. Brain Res. Rev. 24, 91–113. [PubMed: 9385453]

Risold PY, and Swanson LW (1997b). Connections of the rat lateral septal complex. Brain Res. Brain Res. Rev. 24, 115–195. [PubMed: 9385454]

Risold PY, Thompson RH, and Swanson LW (1997). The structural organization of connections between hypothalamus and cerebral cortex. Brain Res. Brain Res. Rev. 24, 197–254. [PubMed: 9385455]

Robertson CE, and Baron-Cohen S (2017). Sensory perception in autism. Nat. Rev. Neurosci. 18, 671–684. [PubMed: 28951611]

Rutishauser U, Mamelak AN, and Schuman EM (2006). Single-trial learning of novel stimuli by individual neurons of the human hippocampus-amygdala complex. Neuron 49, 805–813. [PubMed: 16543129]

Salay LD, Ishiko N, and Huberman AD (2018). A midline thalamic circuit determines reactions to visual threat. Nature 557, 183–189. [PubMed: 29720647]

Schumacher A, Villaruel FR, Ussling A, Riaz S, Lee ACH, and Ito R (2018). Ventral hippocampal CA1 and CA3 differentially mediate learned approach-avoidance conflict processing. Curr. Biol. 28, 1318–1324.e4. [PubMed: 29606418]

Shang C, Chen Z, Liu A, Li Y, Zhang J, Qu B, Yan F, Zhang Y, Liu W, Liu Z, et al. (2018). Divergent midbrain circuits orchestrate escape and freezing responses to looming stimuli in mice. Nat. Commun. 9, 1232. [PubMed: 29581428]

Sheehan TP, Chambers RA, and Russell DS (2004). Regulation of affect by the lateral septum: implications for neuropsychiatry. Brain Res. Brain Res. Rev. 46, 71–117. [PubMed: 15297155]

Solomon PR (1977). Role of the hippocampus in blocking and conditioned inhibition of the rabbit's nictitating membrane response. J. Comp. Physiol. Psychol. 91, 407–417. [PubMed: 404342]

Stamatakis AM, and Stuber GD (2012). Activation of lateral habenula inputs to the ventral midbrain promotes behavioral avoidance. Nat. Neurosci. 15, 1105–1107. [PubMed: 22729176]

Strange BA, Witter MP, Lein ES, and Moser EI (2014). Functional organization of the hippocampal longitudinal axis. Nat. Rev. Neurosci. 15, 655–669. [PubMed: 25234264]

Thompson CL, Pathak SD, Jeromin A, Ng LL, MacPherson CR, Mortrud MT, Cusick A, Riley ZL, Sunkin SM, Bernard A, et al. (2008). Genomic anatomy of the hippocampus. Neuron 60, 1010–1021. [PubMed: 19109908]

Tingley D, and Buzsáki G (2018). Transformation of a spatial map across the hippocampal-lateral septal circuit. Neuron 98, 1229–1242.e5. [PubMed: 29779942]

Tingley D, and Buzsáki G (2020). Routing of hippocampal ripples to subcortical structures via the lateral septum. Neuron 105, 138–149.e5. [PubMed: 31784288]

Todorovic C, Radulovic J, Jahn O, Radulovic M, Sherrin T, Hippel C, and Spiess J (2007). Differential activation of CRF receptor subtypes removes stress-induced memory deficit and anxiety. Eur. J. Neurosci. 25, 3385–3397. [PubMed: 17553007]

Treit D, and Pesold C (1990). Septal lesions inhibit fear reactions in two animal models of anxiolytic drug action. Physiol. Behav. 47, 365–371. [PubMed: 1970655]

van der Veldt S, Etter G, Mosser CA, Manseau F, and Williams S (2021). Conjunctive spatial and self-motion codes are topographically organized in the GABAergic cells of the lateral septum. PLoS Biol. 19, e3001383. [PubMed: 34460812]

Van Pett K, Viau V, Bittencourt JC, Chan RK, Li HY, Arias C, Prins GS, Perrin M, Vale W, and Sawchenko PE (2000). Distribution of mRNAs encoding CRF receptors in brain and pituitary of rat and mouse. J. Comp. Neurol. 428, 191–212. [PubMed: 11064361]

Vazey EM, Moorman DE, and Aston-Jones G (2018). Phasic locus coeruleus activity regulates cortical encoding of salience information. Proc. Natl. Acad. Sci. USA 115, E9439–E9448. [PubMed: 30232259]

Vertes RP (1992). PHA-L analysis of projections from the supramammillary nucleus in the rat. J. Comp. Neurol. 326, 595–622. [PubMed: 1484125]

Vinogradova OS (2001). Hippocampus as comparator: role of the two input and two output systems of the hippocampus in selection and registration of information. Hippocampus 11, 578–598. [PubMed: 11732710]

Vinogradova OS, and Brazhnik ES (1978). Neuronal aspects of septo-hippocampal relations. In Functions of the Septo-Hippocampal System (Elsevier), pp. 145–170.

von Reyn CR, Nern A, Williamson WR, Breads P, Wu M, Namiki S, and Card GM (2017). Feature integration drives probabilistic behavior in the Drosophila escape response. Neuron 94, 1190–1204.e6. [PubMed: 28641115]

Wall NR, Wickersham IR, Cetin A, De La Parra M, and Callaway EM (2010). Monosynaptic circuit tracing in vivo through Cre-dependent targeting and complementation of modified rabies virus. Proc. Natl. Acad. Sci. USA 107, 21848–21853. [PubMed: 21115815]

Watabe-Uchida M, Zhu L, Ogawa SK, Vamanrao A, and Uchida N (2012). Whole-brain mapping of direct inputs to midbrain dopamine neurons. Neuron 74, 858–873. [PubMed: 22681690]

Wickersham IR, Lyon DC, Barnard RJO, Mori T, Finke S, Conzelmann KK, Young JAT, and Callaway EM (2007). Monosynaptic restriction of transsynaptic tracing from single, genetically targeted neurons. Neuron 53, 639–647. [PubMed: 17329205]

Wirtshafter HS, and Wilson MA (2019). Locomotor and hippocampal processing converge in the lateral septum. Curr. Biol. 29, 3177–3192.e3. [PubMed: 31543450]

Wirtshafter HS, and Wilson MA (2020). Differences in reward biased spatial representations in the lateral septum and hippocampus. Elife 9, e55252. [PubMed: 32452763]

Wirtshafter HS, and Wilson MA (2021). Lateral septum as a nexus for mood, motivation, and movement. Neurosci. Biobehav. Rev. 126, 544–559. [PubMed: 33848512]

Wong LC, Wang L, D'Amour JA, Yumita T, Chen G, Yamaguchi T, Chang BC, Bernstein H, You X, Feng JE, et al. (2016). Effective modulation of male aggression through lateral septum to medial hypothalamus projection. Curr. Biol. 26, 593–604. [PubMed: 26877081]

Xu Y, Lu Y, Cassidy RM, Mangieri LR, Zhu C, Huang X, Jiang Z, Justice NJ, Xu Y, Arenkiel BR, and Tong Q (2019). Identification of a neuro-circuit underlying regulation of feeding by stress-related emotional responses. Nat. Commun. 10, 3446. [PubMed: 31371721]

Yadin E, and Thomas E (1981). Septal correlates of conditioned inhibition and excitation in rats. J. Comp. Physiol. Psychol. 95, 331–340. [PubMed: 6262389]

Yamagata T, Kahn MC, Prius-Mengual J, Meijer E, Šabanović M, Guillaumin MCC, van der Vinne V, Huang YG, McKillop LE, Jagannath A, et al. (2021). The hypothalamic link between arousal and sleep homeostasis in mice. Proc. Natl. Acad. Sci. USA 118, e2101580118. [PubMed: 34903646]

Yeates DCM, Leavitt D, Sujanthan S, Khan N, Alushaj D, Lee ACH, and Ito R (2022). Parallel ventral hippocampus-lateral septum pathways differentially regulate approach-avoidance conflict. Nat. Commun. 13, 3349. [PubMed: 35688838]

Yilmaz M, and Meister M (2013). Rapid innate defensive responses of mice to looming visual stimuli. Curr. Biol. 23, 2011–2015. [PubMed: 24120636]

Zemanick MC, Strick PL, and Dix RD (1991). Direction of transneuronal transport of herpes simplex virus 1 in the primate motor system is strain-dependent. Proc. Natl. Acad. Sci. USA 88, 8048–8051. [PubMed: 1654557]

Highlights

- LS^{Crhr2} neural activity engaged by threat not reward and predicts defensive responses
- LS^{Crhr2} neurons control behavioral responsivity to discrete threat-related stimuli
- LS^{Crhr2} neurons send higher-order projections to neocortical targets
- LS^{Crhr2} neural activity is aversive, drives arousal, and evokes cortical activation

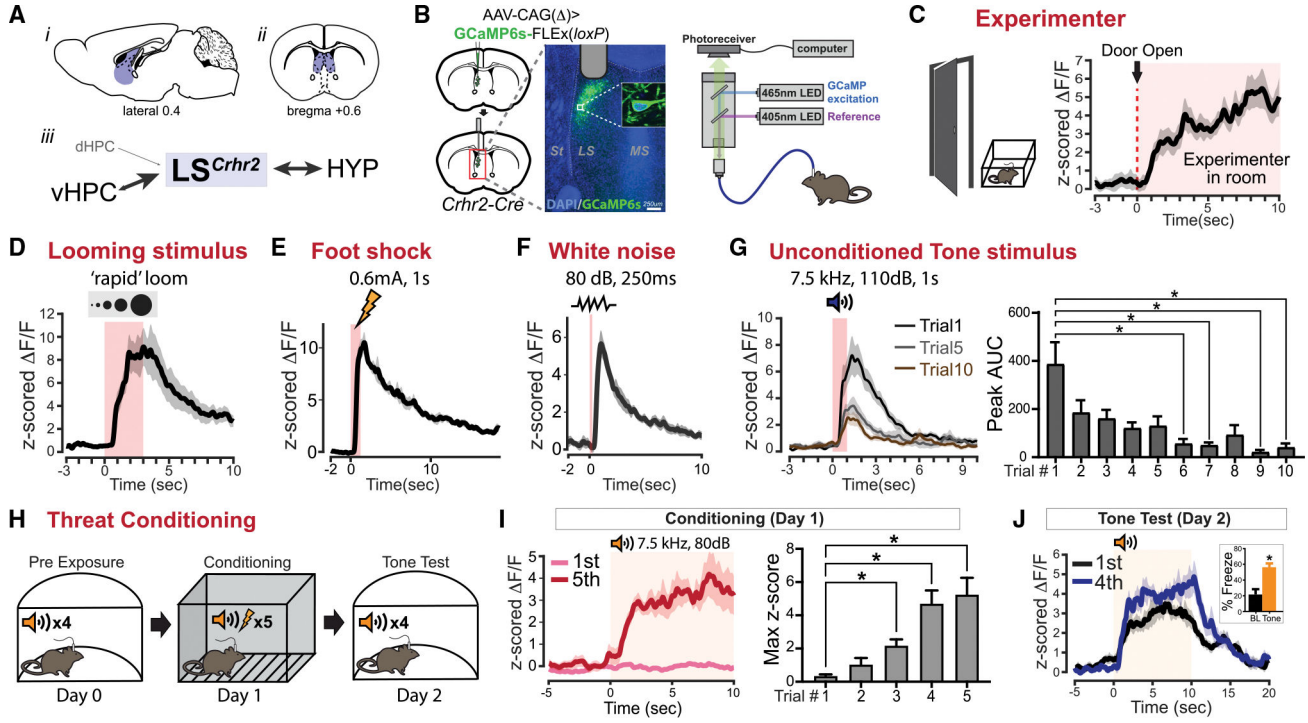

Figure 1. LS^{Crhr2} neurons are phasically activated by unexpected and/or threat-associated sensory stimuli across multiple modalities

(A) Sagittal (i) and coronal (ii) diagrams showing location of LS (blue shading) in subcortical forebrain, and (iii) major connections of LS^{Crhr2} neurons, based on anterograde (Anthony et al., 2014) and retrograde (Figure S1) genetic tracing studies.

(B) GCaMP6s expression in LS^{Crhr2} neurons and fiber photometry recording.

(C–F) Multiple salient and/or threat-associated stimuli phasically activate LS^{Crhr2} neurons upon initial presentation, including approach of laboratory personnel (C; n = 6), looming stimuli (D; n = 12), footshock (E; n = 5), and white noise (F; n = 8). Traces show mean ± SEM of *Z*-scored ΔF/F (normalized fractional change in fluorescence).

(G–J) Unconditioned tones evoke LS^{Crhr2} activity, but responses habituate with repeated unreinforced presentations (G; n = 13). In contrast, tone responses increase across trials when paired with footshock (H and I), and remain high in subsequent tone testing (J; n = 5). One-way repeated-measures AVOVA with Dunnett's multiple comparisons test. Inset, percentage freeze in tone test, baseline (BL) versus conditioned tone, paired t test, *p < 0.05; histograms show mean ± SEM.

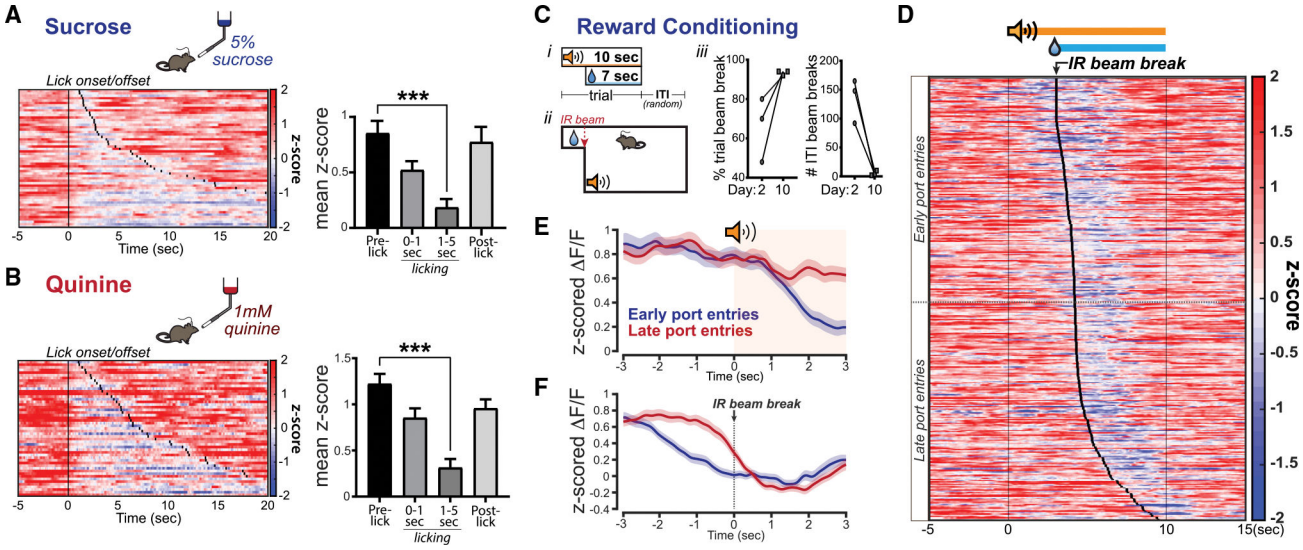

Figure 2. LS^{Crhr2} neurons are suppressed during consummatory behavior and unresponsive to reward-predictive stimuli

(A and B) *Z*-scored ΔF/F for each incidence (rows) of sucrose (A) or quinine (B) consumption from a lickometer; vertical line at t = 0 indicates lick onset, and black ticks indicate lick offset. Neural activity was suppressed during prolonged consumption, an effect that rapidly reversed following cessation of licking. Kruskal-Wallis with Dunn's multiple comparisons test, ***p < 0.001; histograms show mean *Z* score ± SEM.

(C) Reward conditioning task to dissociate neural activity responses to reward-associated stimuli from those to consummatory behavior. Water-restricted mice were trained daily in a task (i) where tone onsets indicated transient availability of water 3 s later from a port; infrared (IR) beam breaks marked port entries (ii). Efficient performance occurred by day 10 (iii), with beam-break probability high during trials but low during intertrial intervals (ITIs).

(D) *Z*-scored ΔF/F for each trial (rows) on day 10 (n = 3 mice); tone onset/offset, vertical lines at t = 0 and 10 s); port entries, black ticks. LS^{Crhr2} activity decreases did not occur phasically in response to tone onsets but rather tracked port entry, a pattern clearest on late port entry trials when tone onsets and beam breaks were temporally well separated.

(E and F) Traces showing mean ± SEM of *Z*-scored ΔF/F for early or late port entries relative to tone onset (E) or beam breaks (F).

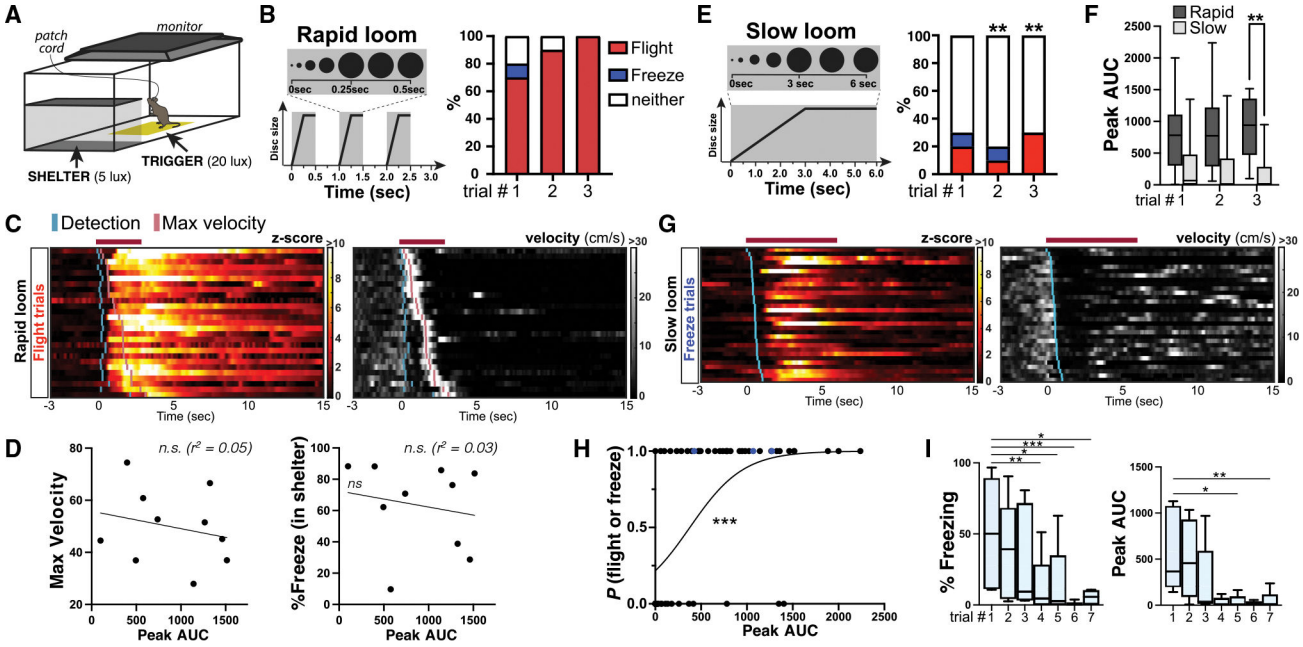

Figure 3. LS^{Crhr2} neural activity is engaged upon detection of perceived threat and predicts probability of defensive behavior

(A) Schematic of looming assay; entry into trigger zone (yellow) results in loom stimulus presentation on overhead monitor.

(B) The first three presentations (trials) of rapid loom stimuli elicited primarily flight into the shelter.

(C) Heat maps of *Z*-scored ΔF/F (left) and velocity (right) responses to rapid loom stimuli on flight trials; teal and pink ticks indicate stimulus detection and maximum velocity, respectively.

(D) Linear regression line slopes for trial #3 flight responses of LS^{Crhr2} activity (peak area under the curve [AUC]) against maximum velocity ($p = 0.52$) or percentage time spent freezing in shelter after flight ($p = 0.61$) are not significantly non-zero, indicating LS^{Crhr2} activity does not directly influence behavioral vigor. Trials 1 and 2 were also non-significant (not shown).

(E) A separate cohort of mice exposed for the first time to slowly expanding loom stimuli (left) exhibited significantly reduced incidence of freezing or flight (right) compared with rapid loom responses plotted in (B) (rapid, n = 10; slow, n = 10; two-sided Fisher's exact test, trial 1 $p = 0.07$, trial 2 $p = 0.001$, trial 3 $p = 0.003$; $^{**}p < 0.01$).

(F) LS^{Crhr2} responses to rapid loom are significantly larger than to slow loom (mixed-effects analysis with Sidak's multiple comparisons test, trial 3 $p = 0.006$).

(G) *Z*-scored ΔF/F (left) and velocity (right) responses to slow loom on trials resulting in freezing not followed by flight; teal ticks indicate stimulus detection.

(H) Logistic regression curve predicting probability of defensive behavior as a function of LS^{Crhr2} population response to looming stimulus exposure. Actual observations (n = 65, data from B and F) plotted as 1 (flight or freezing, n = 36) or 0 (no flight or freezing, n = 29); three freeze datapoints are shown in blue, all other responses were flight. Model slope ($\beta 1 = 1.00342$) is significantly different than 0 (log likelihood ratio = 28.5211, $p < 0.001$) and

receiver operating characteristic (ROC) curve AUC significantly different from 0.5 (0.8860, $p < 0.001$), indicating that magnitude of LS^{Crhr2} activity responses to loom stimuli is related to probability of flight or freezing.

(I) In a separate cohort of mice exposed to repeated slow loom stimuli to elicit habituation, LS^{Crhr2} neural responses decreased in parallel to reductions in defensive behavior ($n = 5$, Friedman tests with Dunn's multiple comparison correction).

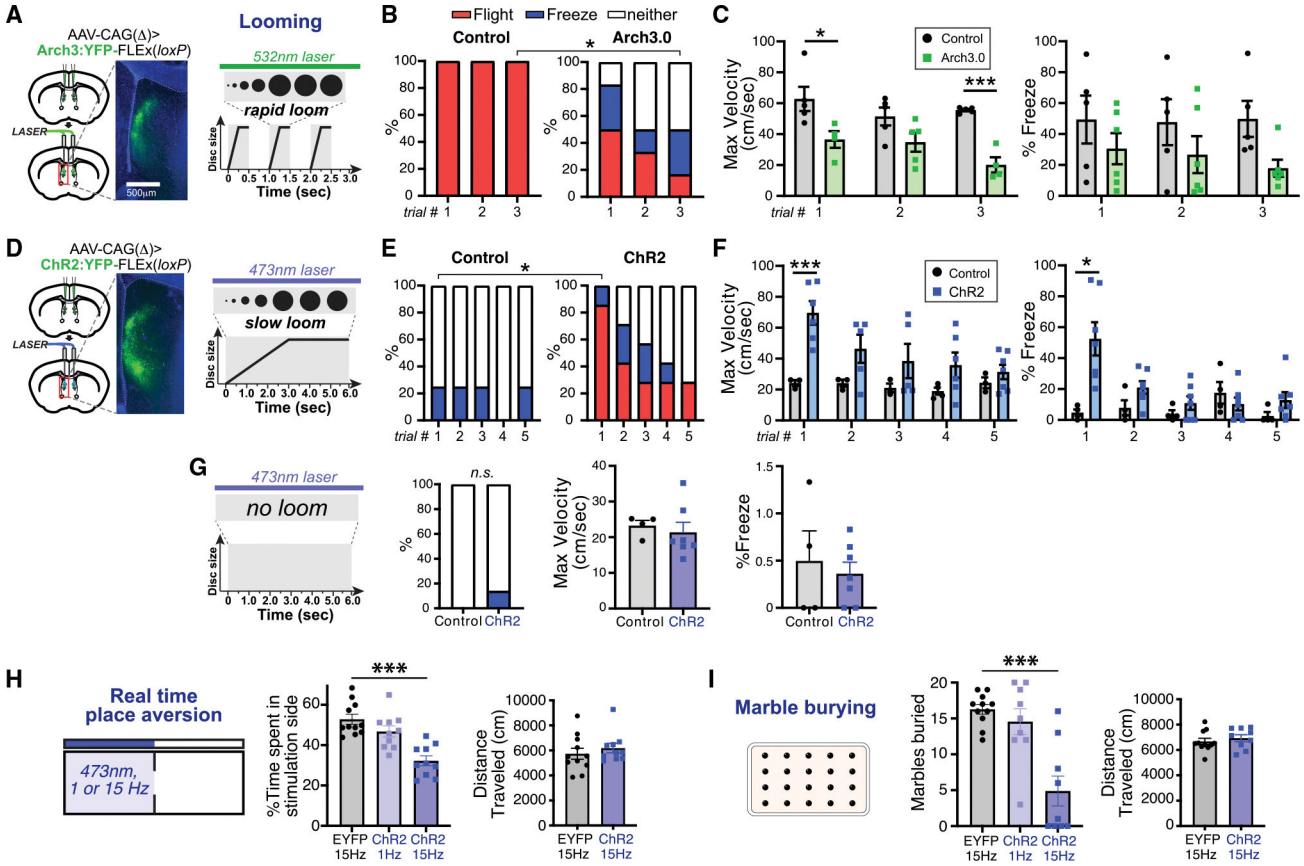

Figure 4. LS^{Crhr2} neuronal activity is necessary for and sufficient to potentiate stimulus-triggered defensive responses but does not evoke specific behaviors

(A) Scheme for optogenetic manipulation (left) and Cre-dependent Arch3:YFP expression in LS^{Crhr2} neurons (right: DAPI, blue; Arch3:YFP, green).

(B and C) Illumination with 532-nm light during rapid loom presentation significantly reduced (B) incidence of flight (control, n = 6; Arch3, n = 6; two-sided Fisher's exact test, trial 3, $p = 0.015$; *$p < 0.05$) and (C, left) maximum velocity exhibited during the first 6 s following light onset (mixed-effects model, group effect, $F(1,8) = 26.43$, $p = 0.0009$; Sidak multiple comparisons test, trial 1 $p = 0.0108$, trial 3 $p = 0.0007$), and a trend toward reduced freezing in the first 20 s following loom stimulus onset (C, right).

(D) Scheme (left) and Cre-dependent ChR2:YFP expression in LS^{Crhr2} neurons.

(E and F) Illumination with 473-nm light (15 Hz, 20-ms pulse width) during slow loom presentation significantly increased (E) incidence of flight (control, n = 4; ChR2, n = 7; two-sided Fisher's exact test, trial 1, $p = 0.015$; *$p < 0.05$), (F, left) maximum velocity exhibited during the first 6 s following light onset (mixed-effects model: group × time interaction, $F(4,26) = 2.949$, $p = 0.0391$; Sidak' multiple comparisons test, trial 1 $p = 0.0009$; ***$p < 0.001$), and (F, right) percentage time freezing in the first 20 s following loom stimulus onset (two-way repeated measures [RM] ANOVA: group effect, $F(1,9) = 5.212$, $p = 0.0483$; group × time interaction, $F(4,36) = 7.849$, $p = 0.0001$; Sidak multiple comparisons test, trial 1 $p < 0.0198$).

(G) Photostimulation of mice in the test arena but without looming stimuli did not elicit any specific behavior or acutely alter mobility.

(H) Photostimulation elicited frequency-dependent avoidance in a real-time place aversion assay without altering distance traveled (EYFP, n = 11; ChR2 1 Hz, n = 10; ChR2 15 Hz, n = 10; percentage time stimulation side, one-way ANOVA with Dunnett's multiple comparison test, EYFP versus ChR2 1 Hz, $p = 0.18$; EYFP versus ChR2 15 Hz, $p < 0.0001$, ***$p < 0.001$; distance traveled, unpaired t test, EYFP versus ChR2 15 Hz, $p = 0.45$).
(I) Photostimulation frequency-dependently suppressed self-initiated marble burying without altering distance traveled (EYFP, n = 11; ChR2 1 Hz, n = 9; ChR2 15 Hz, n = 9; marbles buried, one-way ANOVA with Dunnett's multiple comparison test, EYFP versus ChR2 1 Hz, $p = 0.65$; EYFP versus ChR2 15 Hz, $p < 0.0001$, ***$p < 0.001$; distance traveled, unpaired t test, EYFP versus ChR2 15 Hz, $p = 0.49$).

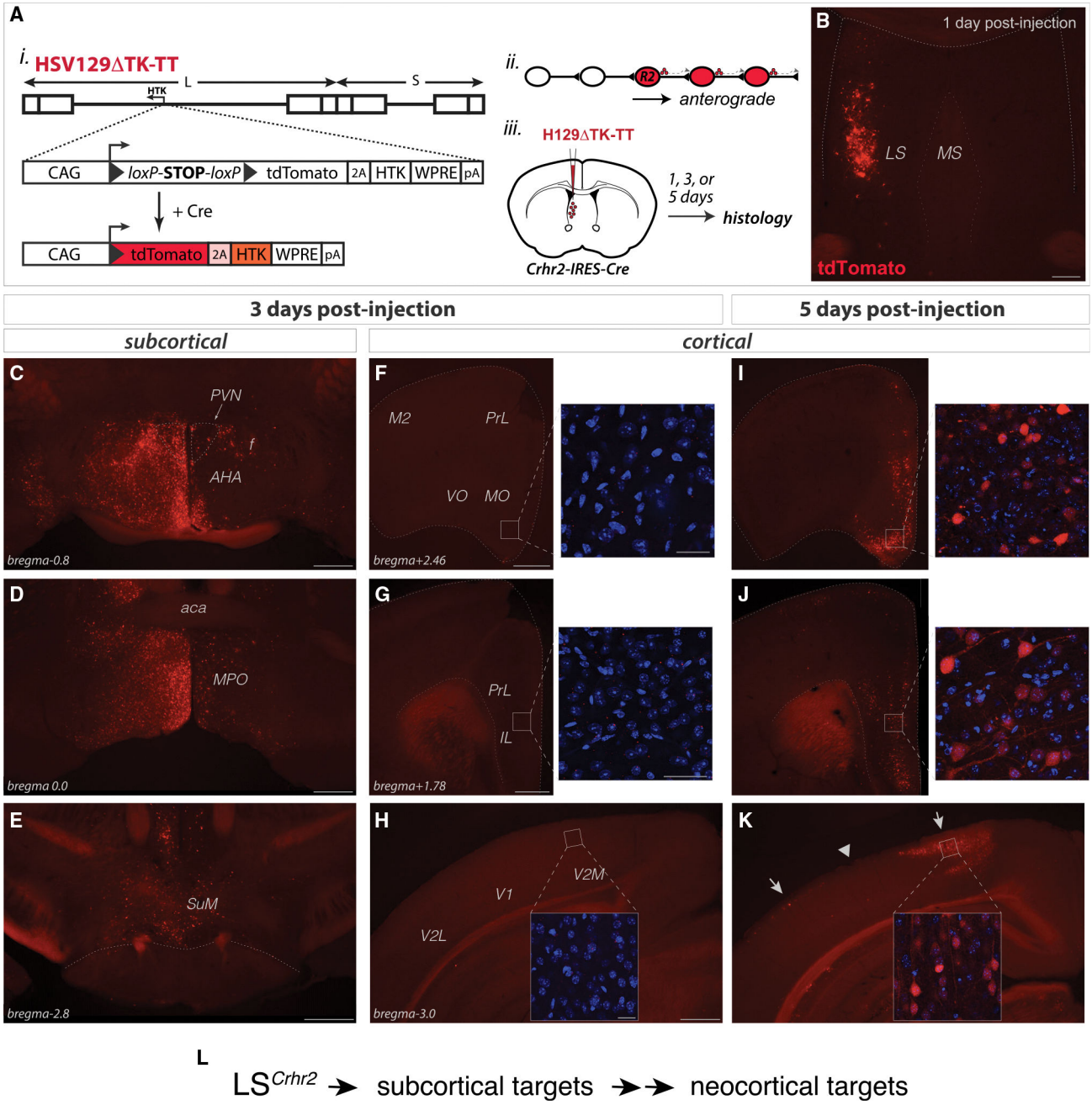

Figure 5. Polysynaptic anterograde transneuronal tracing indicates that LS^{Crhr2} neurons indirectly project to discrete neocortical targets

(A) HSV129ΔTK-TT (i) moves transneuronally in the anterograde direction following Cre-mediated recombination (ii). This vector was injected into LS of *Crhr2*-IRES-Cre mice, and brains harvested at 1 (n = 5), 3 (n = 9), or 5 (n = 7) days post injection (dpi) (iii).

(B) At 1 dpi, robust tdTomato expression was detected in LS but not adjacent regions (medial septum [MS]) or other subcortical areas (Figure S6).

(C–H) At 3 dpi, strong labeling was observed in multiple subcortical regions (C–E) but not neocortex (F–H).

(I–L) By 5 dpi, viral marking was detectable in discrete neocortical regions, including orbitofrontal (I), prefrontal (J), and medial as well as lateral areas of V2 (arrows, K) but not V1 (arrowhead, K; Figure S6E). These data suggest that LS^{Crhr2} neurons send multisynaptic projections to discrete neocortical regions via subcortical intermediates (L). Boxed regions in (F)–(K) shown at high magnification in insets. Red, tdTomato; blue, DAPI.
AHA, anterior hypothalamic area; IL, infralimbic cortex; M2 secondary motor cortex; MO, medial orbital cortex; MPO, medial preoptic area; PrL, prelimbic cortex; PVN, paraventricular nucleus; SuM, supramammillary area; V1, primary visual cortex; V2L/M, lateral/medial areas of secondary visual cortex; VO, ventral orbital cortex. Scale bars (gray bars, lower right): 500 μm (C–K); 250 μm (B); 25 μm (insets, F–K).

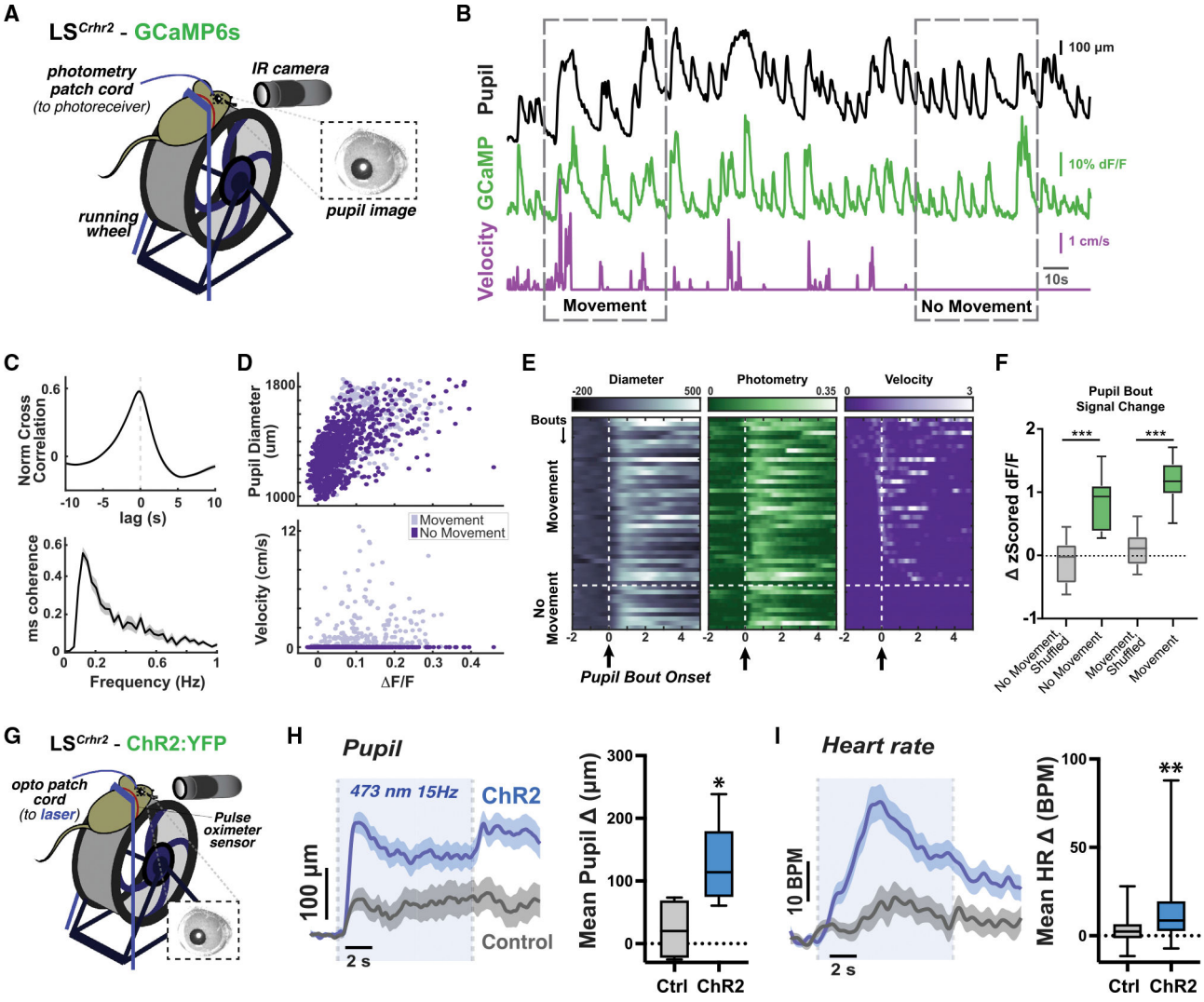

Figure 6. Activity of LS^{Crhr2} neurons tracks brain state fluctuations and drives physiological arousal

(A) Head-fixed setup for fiber photometry recording during pupillometry.

(B) Representative pupil (top, black), LS^{Crhr2} photometry (middle, green), and velocity (bottom, purple) traces during baseline pupillometry recordings in the absence of stimuli. Pupil diameter and LS^{Crhr2} photometry signal correlations are evident irrespective of movement.

(C) Cross correlation and coherence of LS^{Crhr2} photometry and pupil signals. Mean maximum cross correlation was 0.58 ± 0.02 with a mean lag of −0.16 ± 0.05 s. LS^{Crhr2} photometry and pupillometry signals show highest coherence at frequencies <0.2 Hz (n = 13).

(D) Scatterplot of LS^{Crhr2} ΔF/F versus pupil diameter (top) and velocity (bottom). LS^{Crhr2} activity correlates with pupil diameter regardless of mobility (ΔF/F versus pupil during movement: Pearson's r = .59, p < 0.0001, ΔF/F versus pupil during no movement: Pearson's r = .50, p < 0.0001).

(E) Extracted pupil bouts (left, gray) and corresponding photometry (middle, green) and velocity (right, purple) measurements for representative mouse. Pupil diameter, photometry signal, and velocity were sorted based on the velocity latency at onset of pupil bout. Regardless of velocity, pupil diameter and LS^{Crhr2} activity increase concurrently.
(F) All pupil dilation bouts were extracted across 13 animals and *Z*-scored ΔF/F calculated as the difference between pre- and post-pupil-dilation bouts. Changes in LS^{Crhr2} signal were compared with a circularly permutated shuffled signal dataset.
(G) Optogenetic stimulation of LS^{Crhr2} neurons during pupillometry, including pulse oximetry sensor collar to measure heart rate.
(H) Pupil dilation in response to photostimulation was significantly larger in mice expressing ChR2 in LS^{Crhr2} neurons than nontransgenic controls (control, n = 4; ChR2, n = 5; Mann Whitney test, *p = 0.032).
(I) Photostimulation significantly increased heart rate in ChR2-expressing LS^{Crhr2} neurons compared with controls (control, n = 19; ChR2, n = 21; Mann Whitney test, **p = 0.007). All plots are mean ± SEM.

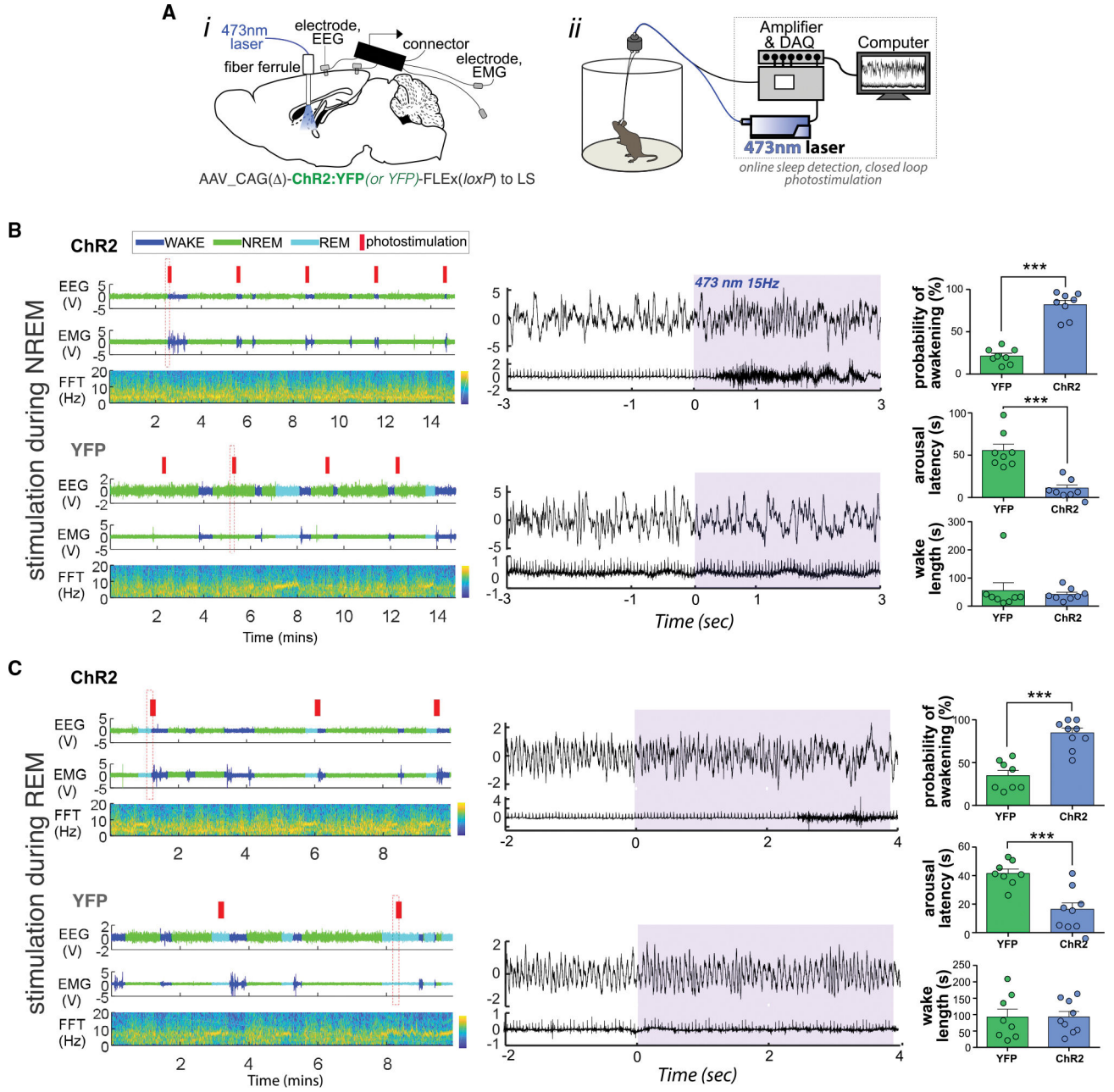

Figure 7. LS^{Crhr2} neurons drive cortical activation in the absence of discrete threat

(A) To assess sufficiency to drive cortical activation, (i) ChR2 or YFP was targeted to LS^{Crhr2} neurons, followed by implantation of a fiber optic ferrule and electrodes for EEG/EMG recording; (ii) mice were subsequently connected to a closed-loop system that delivered optogenetic stimulation when mice were in NREM or REM sleep.

(B and C) Left, representative sleep-wake recordings from ChR2 (upper) or YFP (lower) groups following optogenetic stimulation during NREM (B) or REM (C); red vertical bars indicate photostimulation. (Middle) Higher temporal resolution of dashed boxed areas in left hand panels illustrating short-latency cortical activation and awakening in ChR2-expressing mice. (Right) Bar graphs showing arousal probability during stimulation, latency to arousal,

and length of wake episodes following stimulation. Bars represent mean ± SEM (n = 8 per group), and individual data points represent mean values for individual mice. Unpaired t test, *p < 0.05, **p < 0.01, ***p < 0.001.

KEY RESOURCES TABLE

REAGENT or RESOURCE	SOURCE	IDENTIFIER
Antibodies		
Anti-RFP rabbit polyclonal antibody	MBL Life Science	Code No. PM005, RRID:AB_591279
Bacterial and virus strains		
AAV5_CAG.Flex.GCaMP6s.WPRE.SV40	Chen etal. (2013)	Addgene 100,842-AAV5
AAV5_CAGΔ-Arch3:YFP-FLEx(*loxP*)	This paper	N/A
AAV9_CAGΔ-ChR2(H134R):YFP-FLEx(*loxP*)	This paper	N/A
AAV9_CAGΔ-EYFP-FLEx(*loxP*)	This paper	N/A
AAV5_CAGΔ-split-TVA:Citrine-FLEx(*loxP*)	This paper	N/A
AAV5_CAGΔ-Rabies G-FLEx(*loxP*)	This paper	N/A
EnvA G-Deleted SADB19 Rabies-mCherry	Osakada et al. (2011)	Salk GT3 Vector Core, Addgene 32,636
H129ΔTK-TT	Lo and Anderson (2011)	NIH CNNV
Experimental models: Organisms/strains		
FVB/NTac mice	Taconic Farms	Order code #044
C57Bl/6NHsd mice	Envigo	FVB-M(F)
FVBB6F1 hybrid mice	Bred in house	RRID:MGI:5,653,121
*Crhr2*α-eGFPCre BAC transgenic mice	Anthony et al. (2014)	N/A
Crhr2-IRES-Cre knockin mice	Prescott et al. (2020)	JAX stock #033728
Recombinant DNA		
Arch3.0:YFP coding sequence	IDT	N/A
Split-TVA:Citrine coding sequence	IDT	N/A
pAAV-CA-FLEX-RG	Watabe-Uchida et al. (2012)	Addgene 38,043
pAAV-EF1a-double floxed-hChR2(H134R)-EYFP-WPRE-hGHpA	Addgene plasmid # 20,298; http://n2t.net/addgene:20298	RRID:Addgene_20298
Software and algorithms		
MATLAB (vR2017b)	Mathworks	RRID:SCR_001622
EthoVision XT	Noldus	RRID:SCR_000441
Spike 2	Cambridge Electronic Design	RRID:SCR_000903
GraphPad Prism (v9)	Graphpad	RRID:SCR_002798
Bonsai (v2.3)	Open Ephys	RRID:SCR_017218
Python	Open Source	RRID:SCR_008394
Custom MATLAB code for analysis	Zenodo	https://doi.org/10.5281/zenodo.7057684